Dynamic Structures of Lunar Plasmas Resulting from Moon-Solar Wind Interaction: New Findings by NOZOMI

FUTAANA YOSHIFUMI

Solar-Planetary Electromagnetism Laboratory
Department of Geophysics
Graduate School of Science
Kyoto University

December 20, 2002

Acknowledgments

The author would like to express his grateful thanks to Prof. Shinobu Machida of Kyoto University for his valuable discussions and his supports throughout the works. The author deeply thanks to Emeritus Prof. T. Araki, Prof. T. Iyemori, Dr. T. Kamei, Dr. M. Takeda, Dr. A. Saito, Dr. M. Nosé, and other colleagues of Solar-Planetary Electromagnetism Laboratory and World Data Center for Geomagnetism, Kyoto. This thesis could not have been completed without their sincere comments and encouragements.

The author is deeply grateful to Prof. T. Mukai of Institute of Space and Astronautical Science (ISAS) and Prof. T. Terasawa of University of Tokyo for valuable comments and advices. The author also appreciates late Prof. T. Yamamoto, Dr. H. Hayakawa, Dr. Y. Saito, Dr. A. Matsuoka for development of the plasma and magnetic field instruments on board NOZOMI and providing the author with their valuable data. Their supports and comments were the necessities for completion of this thesis.

The author also thanks the ACE MAG instrument team, ACE SWEPAM instrument team and the ACE Science Center for providing the solar wind data.

Contents

Abstract

The primary subject of this thesis is the plasma environment in the vicinity of the Moon. The study is based on the in situ observations made by particle energy spectrum analyzers mounted on NOZOMI spacecraft at the time of its second lunar swing-by on Dec. 18, 1998.

The nonthermal ions were detected by Particle Spectrum Analyzer/Ion Spectrum Analyzer(PSA/ISA) on board NOZOMI. The data of 3-D velocity distribution functions of the nonthermal ions were analyzed and we found the following characteristics: the nonthermal ions had a partial ring structure in the velocity phase space, they were protons, their source location was the dayside of the Moon, and they had large velocities when they were generated.

The fact that the solar wind protons are reflected in the vicinity of the Moon implies the existence of some dynamic structure such as a small-scale shock associated with a local magnetic anomaly at the lunar surface. We propose the following scenario of the solar wind interaction with the Moon which successfully explains the observed characteristics of the nonthermal protons. When the solar wind protons are deflected by the dynamic structure in the vicinity of the Moon, the first adiabatic invariant is violated. After the deflection, they move under the force of the convection electric field and gyrate around the solar wind magnetic field. This motion forms a partial ring structure with large initial velocities in the velocity phase space.

Backstreaming electrons were also detected by Particle Spectrum Analyzer/Electron Spectrum Analyzer (PSA/ESA) during NOZOMI's second lunar swing-by. From the characteristics of the electron distribution function, we can categorize these events into two types: (1) backstreaming electrons exhibiting a velocity distribution similar to that of the solar wind electrons, but its phase space density ratio to the solar wind electrons decreases as a function of velocity; (2) backstreaming electrons which are thermalized and have a flux comparable to or dominating that of the solar wind electrons.

We considered possible source locations as well as possible mechanisms that can produce these backstreaming electrons. After careful investigations of the velocity distribution function of the electrons and the magnetic field orientation, we concluded that the origin of backstreaming electrons observed in the first event is the lunar wake region, where the electrostatic potential drop associated with the ambipolar plasma expansion reflects the solar wind electrons. The energy of the reflected electrons reaches 480 eV, so that the magnitude of ambipolar electrostatic potential is estimated to be at least 480V.

As for the second event, the electron energy spectrum implies that the solar wind electrons have thermalized at the downstream region. There are two candidates for the thermalization mechanisms; the terrestrial bow shock and the interaction region of the solar wind ions in the downtail of the Moon. When solar wind protons passing both side of the terminator of the Moon interact with each other behind the void region, the two-stream instability can easily develop. After the thermalization of the solar wind electrons, the considerable amount of the solar wind electrons can be reflected back. Both cases can account for the observed counterstreaming electrons of the second event.

Detailed dynamic structures of lunar plasma environment are revealed by the observations by modern instruments on board NOZOMI. The ion observations proved the existence of dynamic structures in front of the Moon. The structures are related to the locally magnetized regions of lunar crustal origin. Our results motivate the theories and numerical modellings of the solar wind interaction with small-scale magnetized region, of which scale is almost of the same order to the gyro-radius of the solar wind protons.

The electron observations detected the large electrostatic potential in the lunar downstream region. The value of 480 V is larger than the value of ∼40 V by numerical calculations. The discrepancy may result from some assumptions made in the calculations. Further studies with more accurate model are necessary for understanding the physics of the lunar wake.

Chapter 1
Introduction

Section 1.1
History of Lunar Plasma Exploration

The lunar exploration can be divided into four phases: 'Pre-Explore 35 Era', 'Explore 35 Era', 'Apollo Era' suggested by *Schubert and Lichtenstein* [1974], and subsequent 'Modern Era'. A brief history of the lunar plasma and the magnetic field exploration is introduced in this section.

1.1.1 Pre-Explore 35 Era

Many satellites have visited the Moon since the USSR Luna 1 fly-by on 1959. The first magnetic field and plasma measurement was conducted by the USSR Luna 2, which impacted the Moon on September 14, 1959. *Dolginov et al.* [1960] claimed that a lunar dipole field would have to have a strength of less than 100 nT at the surface. *Michel* [1964] suggested two simple models of the lunar magnetic field environment. The first model was that the Moon is a perfect insulator. In this case, the magnetic field is not affected by the lunar body so that no global magnetic disturbances cannot be created. Moreover, the absorption of the solar wind plasma into the lunar surface makes a void region behind the Moon. The other model was that the Moon has infinite electric conductivity. In this case, because no magnetic fields penetrate into the lunar body, the magnetic fields pile up and global magnetic disturbances are formed and develop global-scale shock waves in front of the Moon.

USSR Luna 10 satellite placed into the lunar orbit and observed the magnetic field (*Dolginov et al.* [1966]) and plasma (*Gringaus et al.* [1966]) on April 1966. *Gringaus et al.* [1966] set the upper limit of lunar ionosphere concentrations to be 100 ions/cc under the assumption that the lunar ionosphere consists of heavy ions with low temperature.

1.1.2 Explorer 35 Orbiter

Formerly, our knowledge of features of the lunar plasma environment was mainly based on the observation by Explorer 35, which was placed into the lunar orbit on July 22, 1967. Two magnetometers on board Explorer 35 observed lunar magnetic field. The upper bound of the lunar global dipole moment were concluded to be 7×10^{-6} (*Sonett et al.* [1967]) and 10^{-5} (*Ness et al.* [1967]) times that of the Earth's dipole moment which is $8.1 \times 10^{22}\,\mathrm{Am}^2$. No perturbations such as shock waves were detected in the upstream region of the Moon. Subsequently, it was concluded that the Moon is an insulator rather than a conductor.

The lunar surface is a good neutralizer of the solar wind plasma because of the absence of the global magnetic field and the ionosphere. It is clear that the absorption of the solar wind plasma creates a large scale downstream modification, namely, a plasma void (*Lyon et al.* [1967]).

A cavity-associated magnetic feature has been discussed by many authors (for example, *Colburn et al.* [1967]; *Ness et al.* [1968]; *Colburn et al.* [1971]). Typical characteristics of the wake-associated magnetic field is an enhancement of the magnetic field magnitude inside of the cavity (plasma umbra), and a decrease near the cavity boundaries (plasma penumbra).

By the comparison between simultaneous data by Explore 33, which was rounded in the

Earth-circling orbit observing the interplanetary space, and Explore 35, which observed lunar cavity, *Taylor et al.* [1968] confirmed that the above characteristic perturbations are certainly the features of the lunar interaction with the solar wind. *Whang and Ness* [1972] studied the increase of the magnetic field intensity in the umbra and its decreases in the penumbra statistically. The umbral increase has positive correlation with the plasma β value and the ratio to the ambient field(ΔB) is calculated to be $\Delta B = \beta \times (0.25 \pm 0.06)$.

Mihalov et al. [1971] and *Sonett and Mihalov* [1972] reported the characteristic increase of the magnetic field exterior of the penumbra, which is called "limb compression" lately. Because the signature appeared when specific regions of the lunar surface were at the limb, they inferred that the magnetized regions of the lunar crust origin were the source of the perturbations.

1.1.3 Apollo Landers and Subsatellites

Apollo 12, 14, 15 and 16 landers have carried magnetometers to the Moon and they measured the local crustal magnetic field. The magnitude was relatively large and the maximum was 327nT. Correlation of the solar wind dynamic pressure and the magnetic pressure were reported by *Dyal et al.* [1973], and they found that the changes of the magnetic pressure were proportional to the solar wind dynamic pressure.

Apollo 15 and Apollo 16 subsatellites measured magnetic field and charged particles at altitudes of about 100 km from the lunar surface. Similar structures to those observed by Explorer 35 were found at the low altitudes of 100 km. Magnetic disturbances resulting from the remanent magnetic field of the crust were observed when the satellite was in the geomagnetic lobe. Contour plot of the remanent magnetic field was made by *Coleman Jr. et al.* [1972] and *Sharp et al.* [1973], but because trajectories of the subsatellites were limited in space, the remanent field was mapped only in the vicinity of the equator.

Russell and Lichtenstein [1975] statistically showed that the limb compressions appear only in specific selenographic regions and that the occurrence of the limb compressions is correlated with the magnetic field strength. They concluded the probable cause of limb compressions is the deflection of the solar wind by the lunar surface magnetic anomalies in the limb region.

1.1.4 Recent Satellite Observations

After the termination of the Apollo mission, only a small number of spacecraft have visited the Moon.

The WIND satellite was launched on Nov. 1, 1994. One of the scientific objectives of WIND is monitoring of the solar wind plasma and interplanetary magnetic field. WIND traversed the lunar wake on Dec. 27, 1994 at the distance of 6.5 lunar radii(R_L). This is the first measurement of the lunar wake using modern plasma instruments. *Ogilvie et al.* [1996] confirmed that the plasma density decreased exponentially as the spacecraft penetrated into the void region. Such a structure is very consistent with a simple theory of the plasma expansion into the vacuum (*Samir et al.* [1983]). They also concluded that the solar wind ions were accelerated along the direction of the magnetic field by ambipolar electric fields of the order of 2×10^{-4}volts/m. *Bosqued et al.* [1996] obtained the electron and ion density to be < 0.5/cc in the lunar wake. ULF wave activity and energetic electron flows were observed by *Farrell et al.* [1996]. ULF waves were active when the satellite was magnetically connected to the lunar wake region.

Lunar Prospector (LP) blasted off to the Moon on Jan. 6, 1998. One of its critical scientific objectives is to map the lunar magnetic fields. A magnetometer and an electron reflectometer was carried to the Moon (*Lin et al.* [1998]; *Hood et al.* [2001]). *Lin et al.* [1998] presented the observational evidence of the interaction between the lunar magnetic anomalies and the solar wind. The observation showed that the increase in the magnetic field related to the magnetic anomaly disappeared when the solar wind dynamic pressure increased. They concluded that the observation of the increase in the magnetic

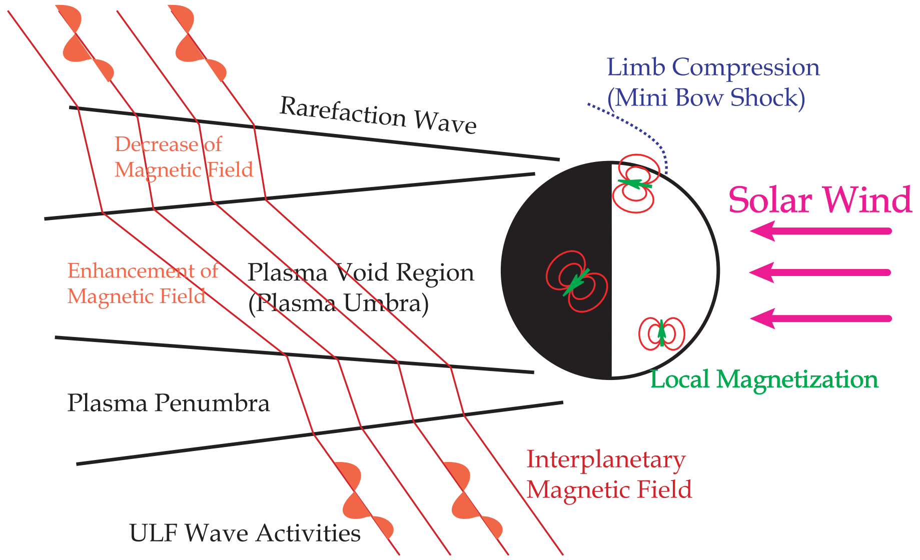

Figure 1.1: A schematic sketch of the plasma and magnetic field environments around the Moon in the solar wind. There are no disturbances in front of the Moon. Local magnetized regions exist at the surface and they may interact the solar wind. A plasma void region is formed behind the Moon and rarefaction waves propagate outward. The magnetic field is increased in the center of the wake and decreased around the void region. ULF waves are found in upstream regions of the central void.

field was due to the pile up of the interplanetary magnetic field.

Section 1.2
Steady States of Moon-Solar Wind Interaction

It is obvious that four different types of the lunar plasma and magnetic field environments can be considered: inside the Earth's plasma sheet, the geomagnetic lobe, the magnetosheath and the solar wind. Few have been studied the interaction with the plasma sheet, in which hot and dense plasma surround the Moon. Because the plasma and magnetic field activity is very small, observations in the geomagnetic lobe are appropriate to understand the lunar remanent magnetic field (e.g., *Coleman Jr. et al.* [1972]) and the inductance (*Hood et al.* [1999]).

The interaction of the Moon with the solar wind has been studied by many authors. Basic features of the interaction with the magnetosheath is almost the same as those with the solar wind. A schematic sketch of the lunar plasma and magnetic field interaction with the solar wind is drawn in Figure 1.1. Steady states of the Moon-solar wind interaction are introduced in the followings.

1.2.1 Lunar Atmosphere and Ionosphere

It is commonly known that the Moon has no atmosphere, but in a strict sense, this statement is not correct. The Moon is surrounded by tenuous collisionless neutral atmosphere. The lunar atmosphere is sometimes called surface boundary exosphere (SBE). Such a structure is also seen in the Mercury and some of the Galileo satellites of Jupiter. Main sources of the lunar atmosphere are the thermal desorption such as adsorption of the lunar regolith, sputtering by solar wind particle and photon, and chemical sources. Loss mechanisms are gravitational escape, chemical loss, condensation and ionization loss (for example, see review by *Stern* [1999]).

Lunar ionosphere is thought to be formed by the photoelectron emitted from the lunar sunlit surface. Dayside photoelectron sheath with a surface density of 10^4 electrons/cc was observed by Apollo observation (*Reasoner and Burke* [1972]). Radio occultation experiments by Luna 22 satellite suggest the existence of the dayside ionosphere with peak densities of 500-1000 electrons/cc at a height of 5-10 km (*Vyshlov* [1976]). If the source of the ionosphere is photoelectron emission, its characteristic thickness is determined by the Debye length. The observed thickness of the photoelectron sheath is too high to explain the source as photoelectron emission from the sunlit surface. The problem still remains as an open question.

1.2.2 Magnetic Field Environment

Early explorations to the Moon have revealed that the Moon has no global dipole field (*Dolginov et al.* [1960]; *Ness et al.* [1967]; *Sonett et al.* [1967]) because the Moon is too small to drive a core dynamo. Moreover, being the Moon body an insulator rather than a conductor, the interplanetary magnetic field can easily penetrate into its inside so that global-scale magnetosphere or bow shock cannot be formed.

Small-scale crustal magnetic fields, called remanent magnetic fields or magnetic anomalies, are distributed, of which spatial scales reach up to 500 km. Large anomalies are mainly distributed in the far-side, namely the invisible side of the Moon. The large anomalies are often in correspondence with the antipodal young impact basin. *Hood and Huang* [1991] implied that an silicate impactor with velocities of 15-20 km/s, which generated a large impact basin, made convergence of plasma cloud and interplanetary magnetic field into the antipodes, and the magnetic field were amplified there.

Limb compression is a magnetic field fluctuation observed at or just in front of the lunar terminator. Because the limb compressions have been observed by many satellites and appeared in specific selenographic regions, *Russell and Lichtenstein* [1975] suggested the correlation between the limb compressions and the lunar surface magnetic anomalies. LP observed magnetic field and electron spectral data being useful to discuss the limb compressions (*Lin et al.* [1998]). When the solar wind dynamic pressure became large, the magnetic field magnification by the limb compression disappeared. They concluded that the signature was due to the deflection of the solar wind and at least one local magnetized region is strong enough to stand off the solar wind and produces shock waves and a small-scale magnetosphere.

Harnett and Winglee [2000] demonstrated the formation of such small scale magnetospheres or shock waves by numerical calculations of hybrid model. They concluded that the formation is realized when the field strength is above 10 nT at 100 km above the lunar surface and when the solar wind ion density is below 40 /cc. They also suggested that

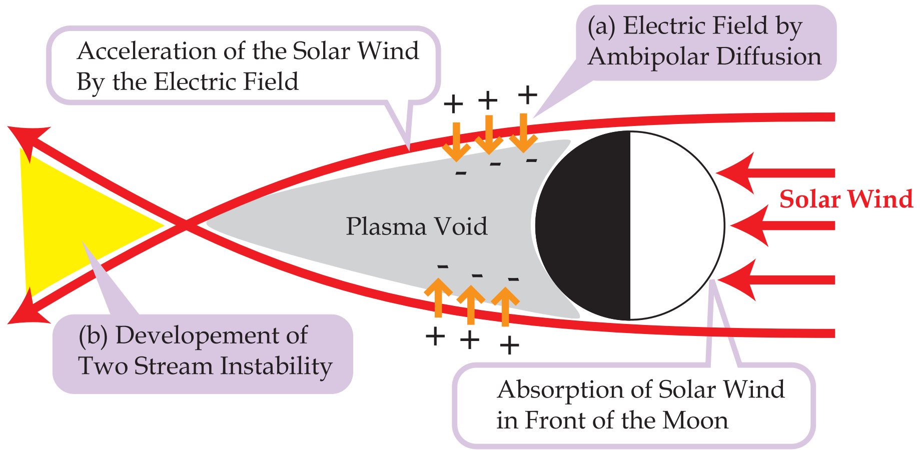

Figure 1.2: Two mechanisms for the generation of the electric field by the interaction between the Moon and the solar wind; (a) Ambipolar diffusion resulting from the difference of the thermal velocities of electrons and ions just behind the lunar terminator. (b) Two stream instability in the downstream wake.

the position and shape of the miniature bow shocks or magnetospheres are dramatically changed by the solar wind conditions.

1.2.3 Lunar Wake

Figure 1.2 is an illustration of behaviors of the solar wind interaction with Moon and generations of electric field in the downstream region of the Moon. A plasma void region are formed behind the Moon because the super-Alfvénic solar wind protons and electrons crash into the lunar surface. Solar wind plasmas traversed beside the Moon will penetrate into the void region in the solar wind frame. Characteristic velocity of the diffusion is determined by the solar wind thermal velocity. Because the thermal velocity of electrons is much larger than that of the ions, the electrons tend to penetrate ahead of the ions. The difference of the penetration velocity into the vacuum causes polarization electric field. The electric field decelerates the electrons and accelerate the ions. In a fluid approximation, the time scale of the diffusion is determined by the ion acoustic velocity (for example, see review by *Samir et al.* [1983]). This process is called ambipolar diffusion.

The ions passed beside the Moon penetrate into the plasma void region by the acceleration of ambipolar electric potential and pressure gradient in the Moon-rest frame. Note that the solar wind bulk velocity is normally larger than that of the ambipolar diffusion. *Ogilvie et al.* [1996] pointed out that a 400-volt ambipolar potential drop is preferable to explain the observed acceleration of the solar wind ions into the lunar wake.

Interaction between the plasma passing one side and that passing the other side of the terminator takes place in the downstream region of the Moon. Two-stream instability easily develops there, so that the large wave electric field can be generated (*Farrell et al.* [1998]). The rarefaction waves expand outside of the void region. The time scale of the expansion is also determined by the ion acoustic velocity. Such regions where the solar wind plasma and magnetic field are drastically modified are called 'lunar wake.'

The magnetic field is increased inside of the lunar void and is decreased just outside of the void region. This is because the total pressure, which is a sum of the magnetic field pressure ($P_B = B^2/2\mu_0$) and plasma thermal pressure ($P_{th} = nkT$) must be conserved through the boundary.

The region magnetically connected to the lunar wake is called 'forewake'. ULF wave activities were observed by WIND satellite (*Farrell et al.* [1996]). The frequency was between 1-2 Hz and coincident energetic electrons were observed. They concluded that the ULF emission was due to the counterstreaming electrons and these observations are very similar to the 'foreshock' region of the Earth's bow shock.

Farrell et al. [1998] simulated the solar wind interaction with the Moon. They were successively realized the rarefaction wave, ambipolar electric fields and ULF wave activities in the forewake in the simulation system. However, the magnitude of ambipolar electric potential and the flux of the counter-streaming electrons observed in the forewake were not described. *Birch and Chapman* [2001] conducted the detailed simulation of the interaction and concluded that the electric potential behind the Moon reaches up to ∼40 volts, which is smaller than that derived by the WIND observation (*Ogilvie et al.* [1996]).

Section 1.3
Ions of Lunar Origin

The Moon has very tenuous atmosphere and ionosphere as described in Section 1.2.1. The ionosphere is too small to carry the diamagnetic current to prevent the solar wind penetration. This means that the ionosphere, the atmosphere and the surface are exposed to the interplanetary medium.

If the ionosphere directly interacts with the interplanetary medium, the ions feel the force by the convective electric field ($\vec{E}_{\mathrm{SW}} = -\vec{V}_{\mathrm{SW}} \times \vec{B}_{\mathrm{SW}}$) and are accelerated to the twice of the solar wind velocity perpendicular to the magnetic field independent of the ion species. Consequently, the ions escape away.

Such ions were observed by AMPTE/IRM satellite (*Hinchenbach et al.* [1991]) and WIND satellite (*Mall et al.* [1998]). *Hinchenbach et al.* [1991] analyzed data by a time-of-flight spectrometer SULEICA on the AMPTE/IRM satellite and detected heavy ions with the mass range between 23 and 37 amu beyond the Earth's bow shock ($\sim 18.7 R_E$ from the Earth). They also reported that the pick-up ions were observed in a period of about 29 days around the new moon. *Mall et al.* [1998] statistically analyzed lunar-originated heavy ions by STICS on the WIND spacecraft. With its 17 lunar fly-bys which took place between 1995 and 1997, lunar originated ions were observed on the earthward side of the Moon as close as 17 lunar radii. The ion species were concluded to be O^+, Al^+, Si^+, and P^+. It must be noticed that these observations was performed in far downstream of the Moon.

The transport of typical ions from the surface of the Moon was calculated by *Cladis et al.* [1994]. They treated the sputtered Si^+ and Ca^+ as test particles and traced their trajectory. They pointed out that the phase space volume of the lunar originated ions were increased due to the diffusion and reflection by the Earth's bow shock and the deflection by the Earth's magnetosphere.

Section 1.4
Objectives of the Thesis

The plasma and the electromagnetic environment of the Moon is obviously different from those of the Earth or Jupiter, which has global magnetic dipole moment, or those of the Mars or Venus, which has ionosphere. Studying the plasma and electromagnetic environments of the Moon will deepen our knowledge on those of Earth from the standpoint of comparative planetology.

Static features of the lunar magnetic field and plasma environment have been explored by many satellites and landers since 1960s. They used fluid models and successively explained the characteristics of the interaction between the Moon and the solar wind.

On the other hand, modern magnetometers and particle spectrometers have higher resolutions in time and in velocity phase space. Understandings of the plasma and electromagnetic field environment around the Earth have much progressed by using such improved instruments. Now it is widely known that kinetic effects of space plasma is important, and sometimes, the kinetic effects control the nature. As a consequence of a termination of lunar explorations in the middle 1970s, observations using modern instruments and non-fluid approach to the lunar plasma environment have become incapable.

When the Moon interacts the solar wind, many dynamic structures are thought to be yielded, for example, interaction of surface materials with the solar wind plasma, the formation of the miniature magnetosphere due to the shielding of the solar wind by the small-scale magnetized regions of crustal origin, the ambipolar diffusion and the rarefaction waves caused by the solar wind plasma penetration into a void region, two-stream instability occurring in the downstream wake, and so on. Studies on the lunar plasma and electromagnetic environments also gave us opportunities to improve understandings on such various topics of the plasma physics.

Japanese NOZOMI satellite was launched on July 4, 1998 and conducted terrestrial swing-by on Dec. 20, 1998 to send onto a transfer orbit to Mars. NOZOMI has experienced lunar swing-by twice before the terrestrial swing-by. The latter swing-by was conducted on Dec. 18, 1998 and the plasma instruments on board NOZOMI could successfully observe the plasma environment of the Moon during the swing-by. This is a rare opportunity to take data in the vicinity of the Moon by modern instruments and to progress the understandings of the lunar plasma environment with high quality data.

The analyses of the data and discussion on the non-fluid plasma behaviors are shown in this thesis. In Chapter 2, a method of estimating the magnetic field orientations by 3-D velocity distribution functions is explained. An accuracy of the estimation is also discussed. The lunar-originated ions are described in Chapter 3. Nonthermal ions, which were observed in the vicinity of the Moon during the lunar swing-by, have a great amount of information on the Moon-solar wind interaction. In Chapter 4, counter-streaming electrons detected during the swing-by are described. The electrons can be used to understand physics of the lunar wake.

Chapter 2
Estimation of Magnetic Field Direction

Section 2.1
Introduction

Interplanetary magnetic field is one of the most important parameters to discuss the physical processes in the space science. Because it is not possible to use magnetic field data during the NOZOMI's lunar swing-by due to the contamination of considerable amount of noises, information on magnetic fields must be obtained in the other ways.

One possible way is to use other satellite data such as ACE or WIND. They have been observed solar wind parameters at the Lagrangian point ($\sim 230R_E$ from the Earth), which is far from the Moon or NOZOMI ($\sim 60R_E$). This is useful but we have to make some assumptions concerning the propagation time or existence of small-scale structures in the solar wind.

As a alternative method, the orientation of the magnetic field can be estimated using 3-D electron velocity distribution function. The method and accuracy of the estimation are explained in the subsequent sections.

Section 2.2
Magnetic Field Data from NOZOMI

Magnetic field observations were performed by NOZOMI magnetic field experiment (MGF) as described in the paper of *Yamamoto and Matsuoka* [1998]. A three-axis flux-gate magnetometer of the MGF is installed at the end of a 5-m deployable mast. However, the mast will not be extended until the insertion of the NOZOMI into Mars orbit, so that the magnetic field data were contaminated by a variety of electromagnetic noises originating from the satellite itself, control units and on board instruments. The noise was especially prominent during the lunar swing-by.

The most significant process to eliminate the noise is the determination of offsets. The offsets vary with the operation modes of the NOZOMI spacecraft. The offsets of the magnetic field perpendicular to the spin axis were eliminated by the considerable efforts of the MGF science team. Magnetic field originating from the satellite body would rotate with spin of the spacecraft. On the other hand, the natural magnetic fields do not rotate with spin. It is possible to determine the offsets using the spin of the spacecraft.

To eliminate the offsets parallel to the spin axis, Davis-Smith method (*Davis and Smith* [1968]) was employed. The method can determine the null point on the assumption that the magnetic field strength is constant during the spin period. Large time scale variations of the magnetic field in the interplanetary medium are mainly Alfvén waves, which do not change the amplitude of the magnetic field. The assumption is approximately valid in the solar wind.

It is possible to obtain the three components of the magnetic field within the error of $\sim$1 nT with a sampling rate of one spin period. However, the error drastically increases when operations of NOZOMI or the other on board instruments are functioned frequently. In particular, the magnetic field data during the lunar swing-by was less reliable (private discussion, A. Matsuoka).

Section 2.3
Estimation by Electron Data

2.3.1 Electrons in Solar Wind

Solar wind plasma is mainly composed of protons and electrons. Low energy solar wind electrons are known to have some components in the solar wind; core, halo, and strahl (for example, *Feldman et al.* [1975]). The core is a thermal component with temperature of 10-20 eV and has the largest density. Electrons with energies of 10 eV have velocities of ~1800 km/s. This means that the thermal velocity of the electron is larger than the bulk velocity of the solar wind (normally 400 km/s).

The halo and the strahl components are suprathermal components. The halo has large temperature anisotropy, namely the temperature parallel ($T_{\parallel}$) and perpendicular ($T_{\perp}$) to the magnetic field differ. Their typical temperature is 60-100 eV. The strahl is a narrow beam, typically 20° of its angular width (*Ogilvie et al.* [1999]), extended along the magnetic field line. The energy is larger than 100 eV. It is known that the amount of the electrons moving away from the sun is larger than that the sunward component.

2.3.2 Electron Temperature Anisotropy

Usually, plasmas have some temperature anisotropies; isotropic, dumbbell-like, pancake-like, and anisotropic distributions. Schematic illustration of the electron velocity distribution functions are shown in Figure 2.1.

The isotropic distribution has the same temperature in any directions. In this case, the estimation of the magnetic field is not possible. Collisional plasma often has the isotropic distribution.

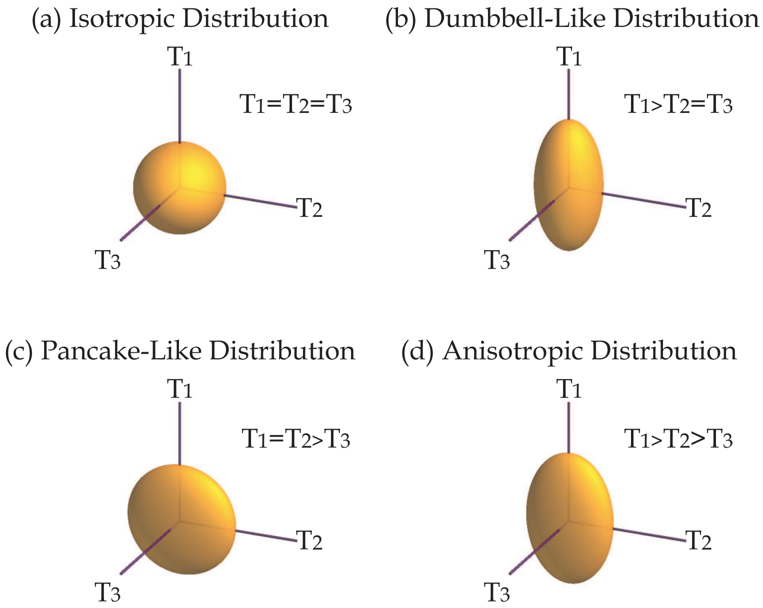

Figure 2.1: Four types of typical temperature anisotropies in the velocity space; (a) isotropic distribution, (b) dumbbell-like distribution, (c) pancake-like distribution and (d) anisotropic distribution . The solar wind electrons with energies > 100 eV have dumbbell-like anisotropy.

Dumbbell-like distribution has a large temperature in one direction and smaller temperature in the remaining two directions ($T_1 > T_2 = T_3$). The magnetic field is parallel to the eigenvector corresponding to the largest temperature axis (T_1) because of the gyrotropic symmetry with respect to the magnetic field. The nonthermal component of solar wind electrons has the dumbbell-like distribution.

Pancake-like distribution has a small temperature in one direction and larger temperature in the other directions ($T_1 = T_2 > T_3$). The magnetic field is thought to be parallel to the eigenvector corresponding to the smallest temperature (T_3) axis. If the isotropic plasma is thermalized in perpendicular directions to the magnetic field, this distribution is produced.

In the case of fully anisotropic distribution with three different temperatures, the magnetic field cannot be determined from the electron data. However, this distribution is not stable because the electrons have symmetry around the magnetic field and if the symmetry has been destroyed, it is restored to be symmetric quickly.

2.3.3 Electron Data from NOZOMI

Particle Spectrum Analyzer/Electron Spectrum Analyzer (PSA/ESA) on board NOZOMI can measure electron counting rate with an energy range from 12 eV to 15 keV (*Machida et al.* [1998]). During the lunar swing-by of NOZOMI, the energy range was set to be from 12 eV to 3 keV. PSA/ESA can cover full 4π steradian in one spin. The angular resolution is 22.5° for elevational and azimuthal directions.

Initial observations and analysis of the electron data obtained in the solar wind revealed that electron data with energies less than 60-80 eV were contaminated by various low energy electrons of non-solar-wind origin such as photoelectrons. They may be generated at the surface of the spacecraft or inside the ESA. In any case, it is difficult to eliminate the photoelectrons. Therefore, only the electrons with energies greater than 100 eV are used in the following analysis. This energy range corresponds to the halo or the strahl components of the solar wind electrons and they are expected to have large temperature anisotropy.

Section 2.4
Method

The suprathermal electrons of the halo and strahl components have a large temperature anisotropy. Normally, the temperature parallel to the magnetic field is higher than the temperature perpendicular to the magnetic field. By calculating the temperature tensor of electrons, the eigenvector for the largest eigenvalue of the three corresponds to the magnetic field orientation.

Temperature tensor is calculated as follows:

$$T_{ij} = \frac{m}{nk}\iiint (v_i - V_i)(v_j - V_j) f(\vec{v}) dv_x dv_y dv_z \tag{2.1}$$

where T_{ij} is the temperature tensor, $f(\vec{v})$ is the electron velocity distribution function, m is an electron mass, and k is the Boltzmann constant. n and $\vec{V}$ is density and bulk velocity of the solar wind calculated by the following equations:

$$n = \iiint f(\vec{v}) dv_x dv_y dv_z, \tag{2.2}$$

$$V_i = \frac{1}{n}\iiint v_i f(\vec{v}) dv_x dv_y dv_z. \tag{2.3}$$

Electrons with energies higher than 100 eV are used for the calculations.

T_{ij} is a symmetric tensor so that T_{ij} can always be diagonalized. T_{ij} have three eigenvalues, T_1, T_2, and T_3 ($T_1 \geq T_2 \geq T_3$). Solar wind electrons with energies larger than 100 eV have the dumbbell-like distribution, so that the eigenvalues T_1, T_2, and T_3 are expected to satisfy $T_1 > T_2 \sim T_3$. The eigenvector corresponding to eigenvalue T_1 is the orientation of the magnetic field.

When electrons do not have the dumbbell-type distribution, the estimations are unreliable. The following criteria were applied to eliminate the data in which the electrons do not have dumbbell-like distribution function.

$$\left(\frac{T_1}{T_2} - 1\right)^2 + \left(\frac{T_2}{T_3} - 1\right)^2 > 0.1^2 \tag{2.4}$$

and

$$\left(\frac{T_1}{T_2} - 1\right) > 2\left(\frac{T_2}{T_3} - 1\right). \tag{2.5}$$

Eq. (2.4) eliminates the case when electron distributions are isotropic and Eq. (2.5) eliminates the case when electron distributions are pancake-like ($T_1 \sim T_2 > T_3$) or fully anisotropic ($T_1 > T_2 > T_3$).

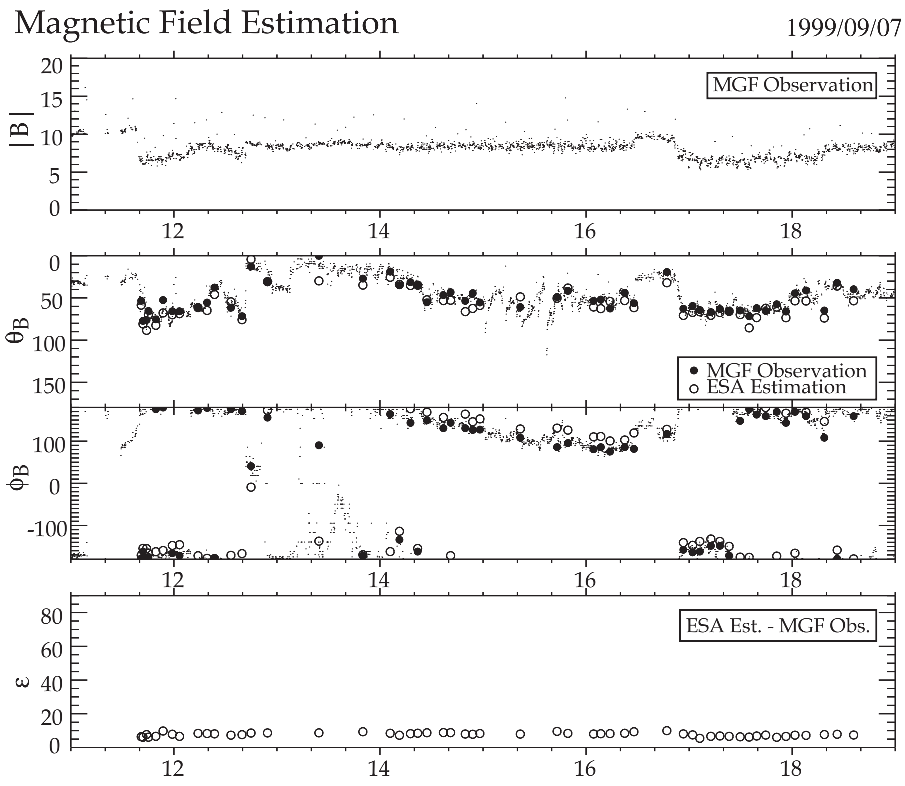

Figure 2.2: Results of the estimation of the magnetic field orientation by electron data. From top to bottom, magnitudes of the magnetic field measured by MGF, the magnetic field directions inferred from MGF data (closed circles) and ESA estimation (open circles), and errors of the estimation are shown.

Section 2.5
Application

2.5.1 Application to Data on Sept. 7, 1999

The above method is applied to the real data obtained by PSA/ESA. The data is compared to the calibrated MGF data for the purpose of confirming the validity of our estimation method.

Figure 2.2 shows a result of the estimation for the data obtained on Sept. 7, 1999.

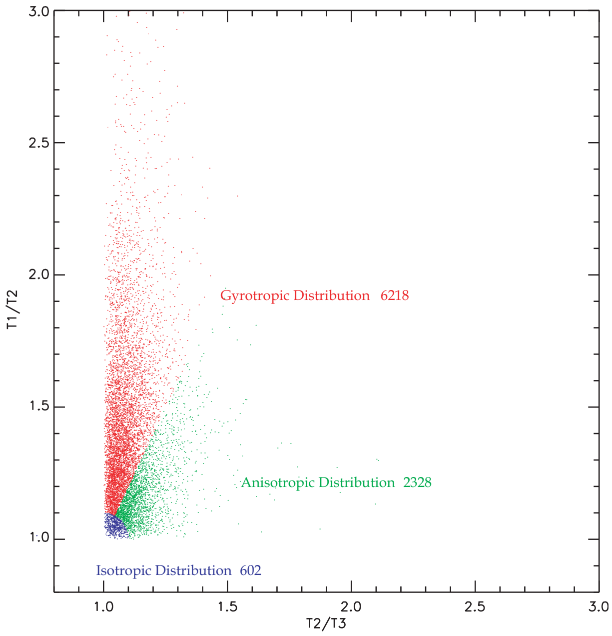

Figure 2.3: Distribution of electron temperature anisotropies calculated by the ESA data. The data cover the period from Aug. 19 to Dec. 31, 1999.

The top panel shows the magnitude of the magnetic field obtained by MGF instrument. The magnitude of $\sim$7 nT is sufficiently larger than the MGF calibration error of $\sim$1 nT.

The second and the third panels show the magnetic field directions in the spacecraft coordinate system. θ represents the angle of the magnetic field vector with respect to the spin axis and ϕ represents the azimuthal angle. Filled and open circles are observational data by MGF and estimated values using electron data, respectively. There is 180° ambiguity, but the polarity of the estimated magnetic field is chosen so as to minimize the deviation of the estimated value from the MGF data.

The bottom panel shows the errors. The value of $\sim$10° for the error is enough small, and it is concluded that the magnetic field orientations can be successfully estimated.

2.5.2 Statistical Evaluation

A forementioned estimation method has been applied to data obtained during the interval between Aug. 19, 1999 and Dec. 31, 1999, when NOZOMI was in the transfer orbit to the Mars. During this interval, NOZOMI observed the solar wind, and three-dimensional electron data of PSA/ESA and magnetic field data of MGF are available.

First, the electron temperature anisotropies are checked. Figure 2.3 is a scatter plot for the electron temperature anisotropies as a function of T_2/T_3 and T_1/T_2. Blue dots correspond the isotropic distribution which does not satisfy Eq. (2.4). Green dots are the pancake-like or anisotropic distribution which does not satisfy Eq. (2.5). The remaining red dots correspond to the dumbbell-like distribution, for which the estimation of the magnetic field orientation is reliable.

Magnetic field orientations were successfully estimated in 6218 samples out of total 9148 samples. Because occasionally there are lacks in the MGF data, 4588 samples were used to analyze the errors of estimation.

Figure 2.4 shows statistical results for the estimation error. The standard deviations of the error are 25° and 33° for θ- and ϕ-component, respectively. The estimation error found to be about the same to the angular resolution of ESA (22.5°)

The histogram of the estimation error taking both θ- and ϕ-components into account, i.e., the relative angle between the estimated and observed magnetic fields, is also shown. We found that 70% of all data was estimated within an error of 27°. The estimation errors are small enough to be used practically. It should be noticed that the calibrated MGF data may have some errors as well, so that the actual error of our estimation should be better than 27°.

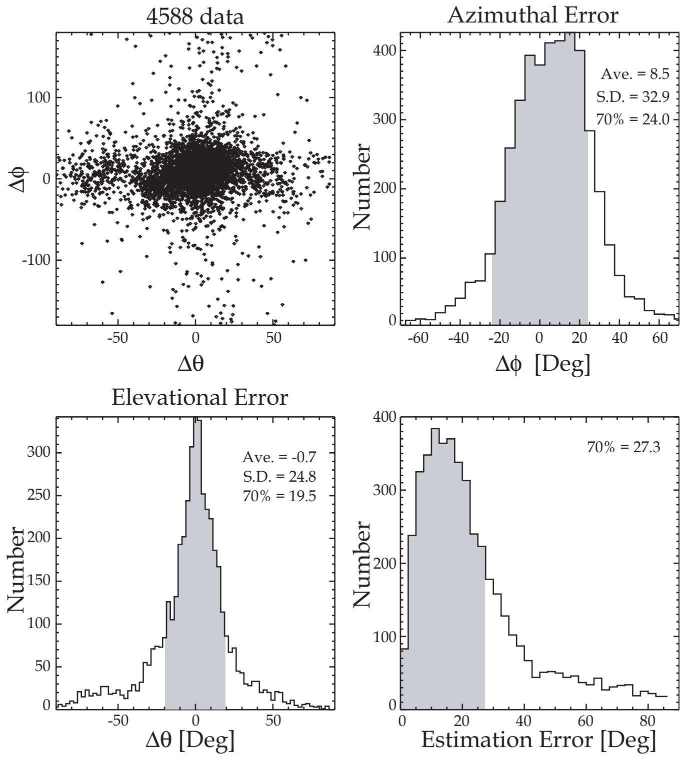

Figure 2.4: The results of the the magnetic field estimation. 4588 samples, for which the magnetic field and three dimensional electron data was available, were used in the analysis. The standard deviations are 33° and 25° for ϕ- and θ-components. 70% of 4588 data can be successfully estimated within an error of 27°.

Section 2.6
Concluding Remarks

A simple estimation method of the magnetic field orientation from electron data were shown and applied to the real data. The results show that the method can estimate the magnetic field orientation with an error less than 27°.

The main cause of the estimation error may be the angular resolution of ESA, which is 22.5°. This value is very close to the estimation error. Another possible cause is a time change of the magnetic field and the electron velocity distribution. The estimation becomes worse when plasma environment is suddenly changed.

The estimated data must be used with some care. For example, it is necessary to check whether electron velocity distribution function has gyrotropic distribution. A comparison with the other spacecraft data is also helpful to check the accuracy of estimation.

Chapter 3

Nonthermal Ions Around the Moon

Section 3.1

Introduction

The solar wind ions have bulk velocities of 300~500 km/s and the thermal velocities of 40~60 km/s under nominal conditions. Ions having different velocities from the solar wind sometimes observed in the interplanetary space. Such ions are called 'nonthermal ions.' Two different types of generation mechanism are possible to create the nonthermal ions.

One is a deformation of the velocity distribution of the solar wind. When a dynamic structure such as a shock wave perturbs the solar wind thermal ions, they are observed as nonthermal ions. The other mechanism is related to a production of new ions. Sputtered ions of the surface materials as well as pickup ions of the ionospheric origin can form the nonthermal ions. Through an analysis of the spacecraft data on the nonthermal ions, we can know dynamic structures and generation mechanisms of such ions in the interplanetary space.

3.1.1 Nonthermal Ions Observed Previously

The nonthermal ions are observed in the upstream supercritical bow shocks. In the case of perpendicular shocks, some of the solar wind ions are reflected by the shock potential inside the shock layer back to the solar wind. They are nonthermal ions found in the upstream region of the shocks (e.g., *Asbridge et al.* [1968]; *Paschmann et al.* [1981]; *Thomsen* [1985]).

The nonthermal ions in the phase space present a partial shell structure or a partial ring structure, i.e., the nonthermal protons occupy partially-filled shell or ring in the velocity space (*Paschmann et al.* [1981]; *Thomsen* [1985]).

Nonthermal ions, both proton and heavy ions like O^+, were also observed in the vicinity of the comet Halley (*Mukai et al.* [1986]; *Terasawa et al.* [1986]). The velocity distribution function of the ions had a partial ring structure in the velocity space as a result of the $\vec{E} \times \vec{B}$-drift after neutral atoms or molecules of cometary origin are ionized.

Unmagnetized planets like Mars or Venus inject ions into the interplanetary space (*Mihalov and Barnes* [1981]; *Lundin et al.* [1989]). When neutral atoms in the exosphere, which are exposed in the solar wind, are ionized, the solar wind electric field accelerate the ionized particles and they are observed as nonthermal ions. The ions are expected to exhibit a partial ring structure.

He^+ ions in the interplanetary space are also found (*Möbius et al.* [1985]; *Noda et al.* [2001]). The He^+ flux is due to the pickup of the gravitationally focused interstellar neutral helium flux on the downwind side of the sun.

3.1.2 Nonthermal Ions of Lunar Origin

The Moon has tenuous atmosphere as described in Section 1.2.1. The lunar atmosphere is variable in time due to the exposure in the interplanetary medium. This means that the nonthermal ions can be observed by the pickup mechanism as seen in the vicinity of comets or unmagnetized planets.

The first measurement of the lunar pickup ions was reported by *Hinchenbach et al.* [1991] and *Hilchenbach et al.* [1993]. They used a time-of-flight spectrometer SULEICA on the AMPTE/IRM satellite in the analysis and detected heavy ions with a mass range between 23 and 37 amu beyond the Earth's bow shock

($\sim 18.7 R_E$ from the Earth). They concluded that the nonthermal components were originated from the Moon for the reason of the high correlation between the appearance of the nonthermal ions and the lunar phase. They claimed that the likely sources were a thin layer of lunar atmosphere or an erosion process on the lunar surface.

The lunar originated heavy ions are statistically analyzed by *Mall et al.* [1998]. They used a mass spectrometer, STICS on the WIND spacecraft. With its 17 lunar fly-bys which took place between 1995 and 1997, lunar originated ions were observed on the earthward side of the Moon as close as 17 lunar radii. The ion species were concluded to be O^+, Al^+, Si^+ and P^+.

Nonthermal ions generated by dynamic structures in the vicinity of the Moon have not been discussed because the Moon has been considered to have no dynamic structures in front of its body. All of the solar wind protons are thought to crash into the lunar surface.

Hood and Williams [1989] calculated trajectories of solar wind protons around the local magnetized regions to evaluate changes of the solar wind flux at the lunar surface by the existence of the small-scale magnetic field. *Harnett and Winglee* [2000] used MHD model to study the interaction between small-scale magnetized regions and the solar wind. Both calculations did not treat nonthermal ions.

In this chapter, NOZOMI's observation and analysis of nonthermal ions in the vicinity of the Moon are reported. The analysis reveals that the species of the nonthermal ions are protons. By particle tracing of the nonthermal ions, the nonthermal ions are found to be generated in the vicinity of the Moon. They have partial ring structures in the velocity space and have large velocities when they are generated. From such characteristics of the nonthermal ions, generation mechanisms of the nonthermal ions are discussed.

Section 3.2
Instrumentation

The 3-D ion observations were performed using a Particle Spectrum Analyzer/Ion Spectrum Analyzer (PSA/ISA) mounted on the NOZOMI spacecraft. The PSA/ISA is an electrostatic energy-per-charge analyzer for ions and can measure ions from 6 eV/q to 16 keV/q in 32 energy steps. The energy range can be changed and was up to 3 keV/q during the lunar swing-by. With one spin rotation ($\sim$ 6.5 sec at the time of a lunar swing-by), the PSA/ISA can cover a full 4π steradian view angle with a $22.5° \times 22.5°$ angular resolution.

The time interval between each 3-D velocity distribution data is not regular due to the telemetry architecture. It is about 1 minute before 7:36 UT, except for the data loss interval between 7:18 UT and 7:24 UT. Between 7:43 UT and 7:47 UT, it is every one spin time period, i.e., 6.5 sec., then it is 2 minutes after 7:54 UT.

Because ISA is not a mass spectrometer, no direct informations on mass are available. This is a significant drawback in observing the nonthermal ions. Some assumptions should be made to overcome this drawback as will be shown.

Section 3.3
Observations

3.3.1 Overview of NOZOMI Observation

Figure 3.1(a) shows locations of the Earth, the Moon, NOZOMI, ACE and the Earth's bow shock based on a model by *Peredo et al.* [1995] in the GSE coordinate system on Dec. 18, 1998. The GSE coordinate system has its x-axis pointing from the Earth toward

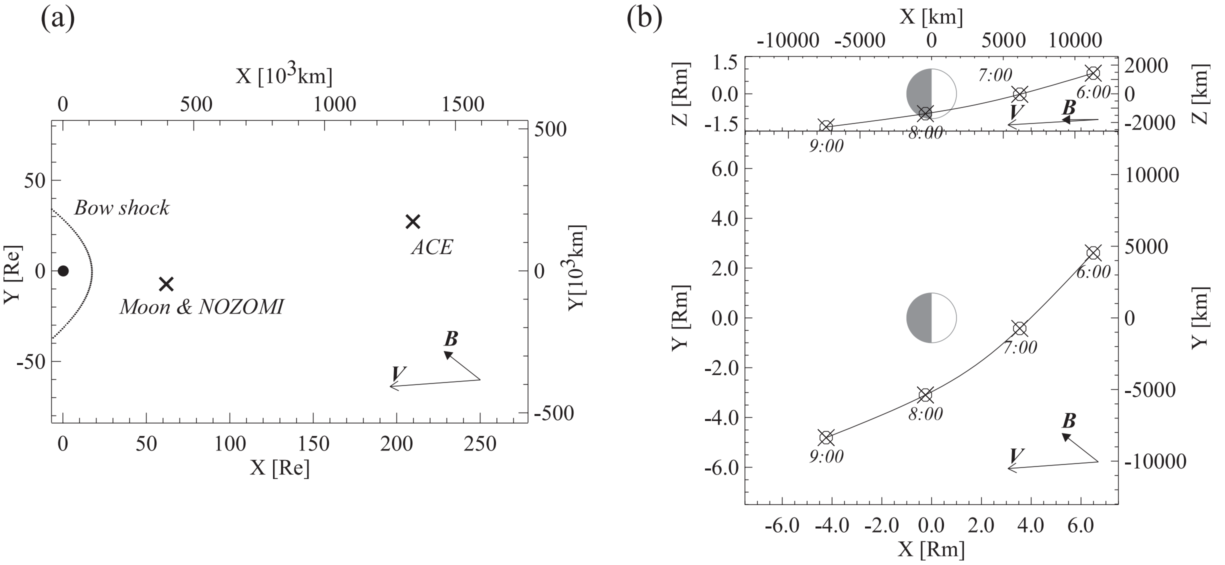

Figure 3.1: (a) Location of the Earth, the Moon, NOZOMI, ACE, and the shape of the Earth's b ow shock modeled by *Peredo et al.*[1995] in the GSE coordinate system. Directions of the averaged magnetic field and the solar wind velocity are also shown. (b) Trajectory of NOZOMI during the lunar swing-by (6:00 UT-9:00 UT) in the LCGSE coordinate system. The circle at the center of each panel represents the Moon. The curve in each panel shows the trajectory of NOZOMI. The closest approach was at 07:34 UT and the distance from the Moon center was ~2,800 km.

the sun, and its y-axis is chosen to be in the ecliptic plane pointing the dawnward of the Earth. z-axis is taken so as to complete the right-handed orthogonal set. The direction of the magnetic field and the solar wind velocity is also indicated. Parameters used to derive the bow shock shape and location are the averaged value of the ACE observation.

The trajectories of the NOZOMI in the Lunar Centered GSE (LCGSE) coordinate system, which is centered on the Moon and has an orientation for each axis that is the same as in the GSE coordinate system, are shown in Figure 3.1(b). The NOZOMI spacecraft approached the Moon at an altitude of approximately 2,800 km at 07:34UT. Because it was a new moon on that day, the Moon was in the solar wind which almost flows along the x-axis.

Figure 3.2 shows a time series of the observation by NOZOMI during the lunar swing-by and the simultaneous observational data by ACE satellite. From top to bottom,

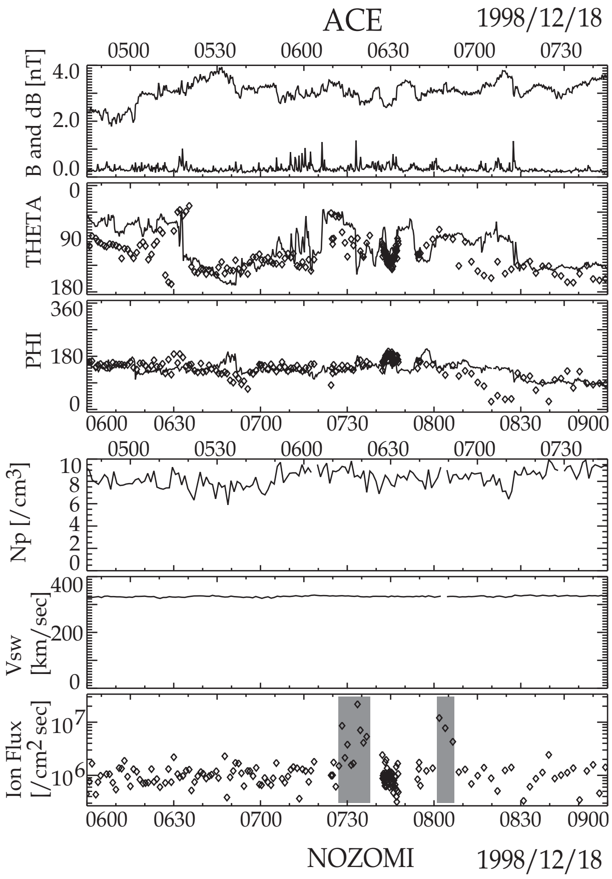

Figure 3.2: Time series of the magnetic field and the plasma moment data obtained by ACE and NOZOMI. From top to bottom, the magnetic field strength and r.m.s., the ratio of those, the θ- and ϕ-components of the magnetic field directions, the solar wind velocity, and the non-solar wind ion flux. The thin lines and the diamond marks in each panel are data obtained by ACE and NOZOMI, respectively. Because NOZOMI's magnetic field data are not available, the direction of the magnetic field was estimated by the electron velocity distribution. The time for ACE and NOZOMI data was shown at the top and bottom of the plot. We assumed the solar wind propagation time to be 75 minutes from the magnetic field direction data,

magnitude and variation of the magnetic field, θ- and ϕ-component of the magnetic field, the proton density, the solar wind velocity, and the nonthermal ion flux observed by NOZOMI. The GSE coordinate system is used in the plot. Solid lines in each panel is data by ACE and diamond symbols represent the NOZOMI data. ACE data is shifted 75 min relative to that of NOZOMI considering the propagation time of the solar wind. NOZOMI magnetic field orientation is estimated by electron data as explained in Chapter 2.

The solar wind condition is very quiet in velocity and magnetic field. No dynamic structures such as interplanetary shocks or CIRs are found during the observation.

Nonthermal ions, in which we are interested, enhanced at around 7:30UT and past 8:00UT. The hatched intervals correspond to the time when the nonthermal ions appeared, and the NOZOMI spacecraft was located very close to the Moon. Their flux is in the order of $10^6/\mathrm{cm}^2$ sec or $10^7/\mathrm{cm}^2$sec, which is one or two orders of magnitude smaller than that of the solar wind.

3.3.2 Characteristics of Nonthermal Ions

Figure 3.3 shows a time series of the ion counts observed by PSA/ISA. From top to bottom, time series of the omnidirectional ion counts, solar wind thermal ion counts, and nonthermal ion counts are shown. A solar wind thermal component is a collimated beam that has a compact volume and has a clear boundary in the velocity phase space, so it is easy to separate the nonthermal component from the thermal one.

The solar wind component has two peaks at velocities of $\sim$350 km/sec and $\sim$500 km/sec; one is for protons and the other is for alpha particles in Figure 3.3(b). The reason why the thermal component shows two peaks will be explained later. Nonthermal ion enhancement around 07:30UT and 08:00UT are also seen in Figure 3.3(c). They have the energies of $\sim$ 1 keV which is as large as the solar wind ions.

The relevant 3-D ion velocity distribution functions are shown in Figure 3.4. The top

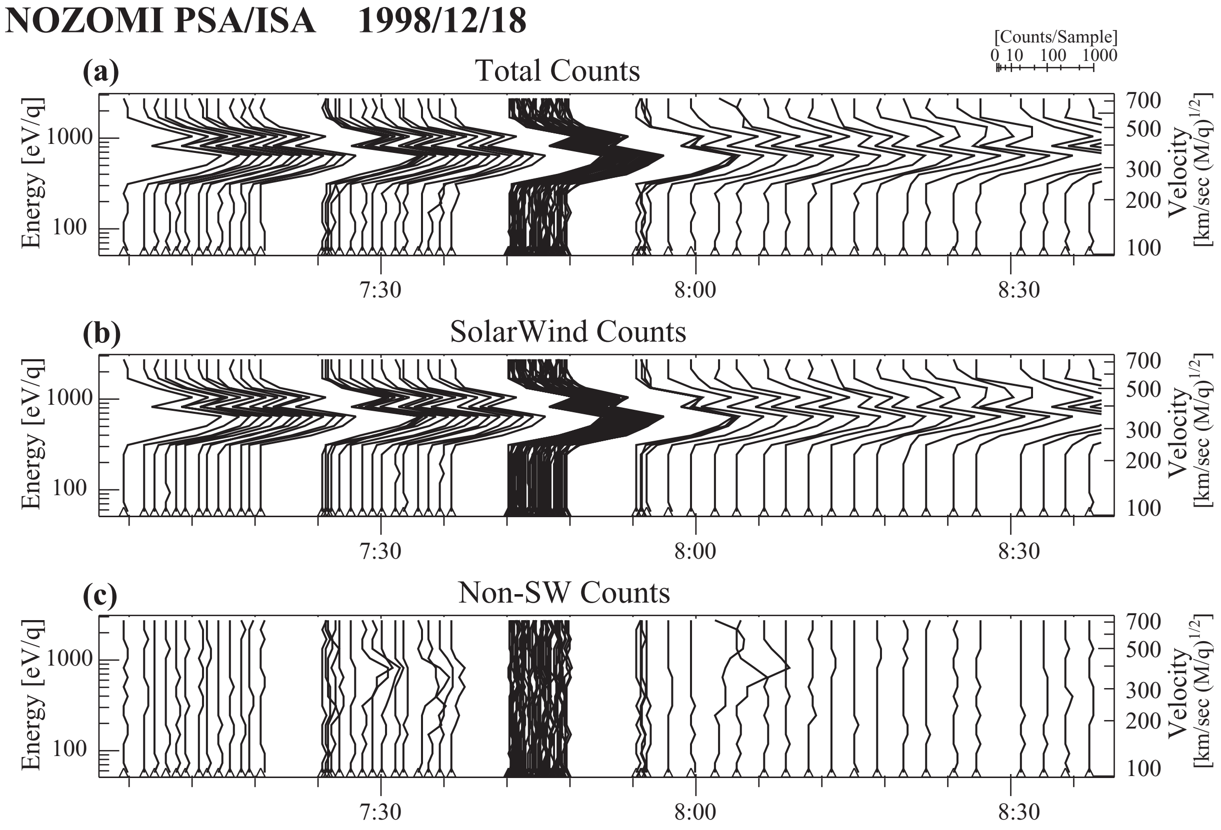

Figure 3.3: Time series of the counting rate observed by PSA/ISA on board NOZOMI. From top to bottom, counting rate for total ions, solar wind ions, and nonthermal ions are plotted. Triangles on the time axis show the time of observation. Two notable peaks in panels (a) and (b) are the solar wind protons and the α particles. Small counts with 10$\sim$20 around 07:30 UT and 08:00 UT are the nonthermal ions. They have almost the same energies as the solar wind protons. Nonthermal ions are clearly absent during 7:40$\sim$08:00 UT.

and bottom panels are for the same time interval for different view angles. The ions with velocities $V_x = -300$ to -500 km/sec are the solar wind ions, which are indicated by red frames. Remaining counts on (b), (c), and (e) are the nonthermal components.

Because PSA/ISA is an energy-per-charge analyzer, we have no information on ion species. Throughout this chapter, we based on the assumption that all ions are protons. This assumption is checked later and is confirmed to be valid.

Figure 3.5 shows the velocity distribution projected onto a plane perpendicular to (a) the direction of the magnetic field and (b) the convection electric field. Here, V_B, V_E, and

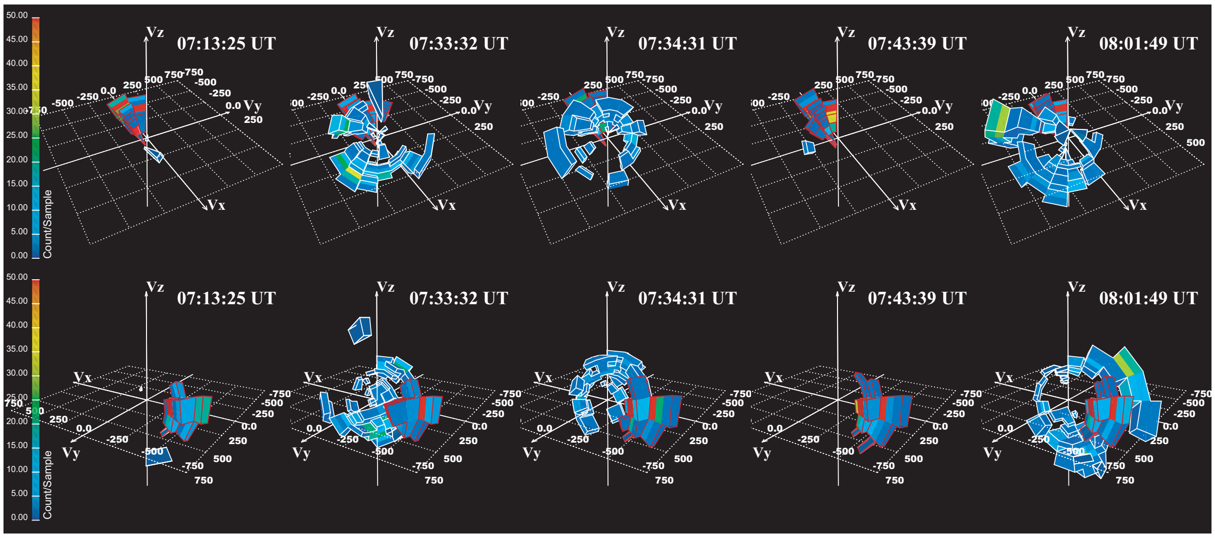

Figure 3.4: Time series of the 3-D velocity distribution in the GSE coordinate system. The upper and lower panels show velocity distributions seen from different angles. The ions with red and white frames are nominal solar wind and nonthermal ions, respectively. The two component can easily be distinguished because the solar wind components are very compact and have clear bound in the velocity space.

V_C represent the velocity parallel to the direction of the magnetic field, the convection electric field, and the $\vec{E} \times \vec{B}$-drift, respectively. The magnetic field direction data are the estimated value by electron data. Partial ring structures can be seen in Figure 3.5 (a) and velocities parallel to the magnetic field are nearly constant in Figure 3.5 (b).

The formation mechanism of the partial ring structure is simple: the ions that have velocities different from solar wind ions start to gyrate around the magnetic field and drift toward the $\vec{E} \times \vec{B}$ direction with the convection electric field $\vec{E} = -\vec{V}_{\mathrm{SW}} \times \vec{B}$. Each ion has a circular trajectory in the $V_E - V_C$ space and the velocity parallel to the magnetic field is preserved. If we observe a limited portion of the ions, we can see a partial ring structure and a relatively constant velocity parallel to the magnetic field as shown in Figure 3.5(a) and (b).

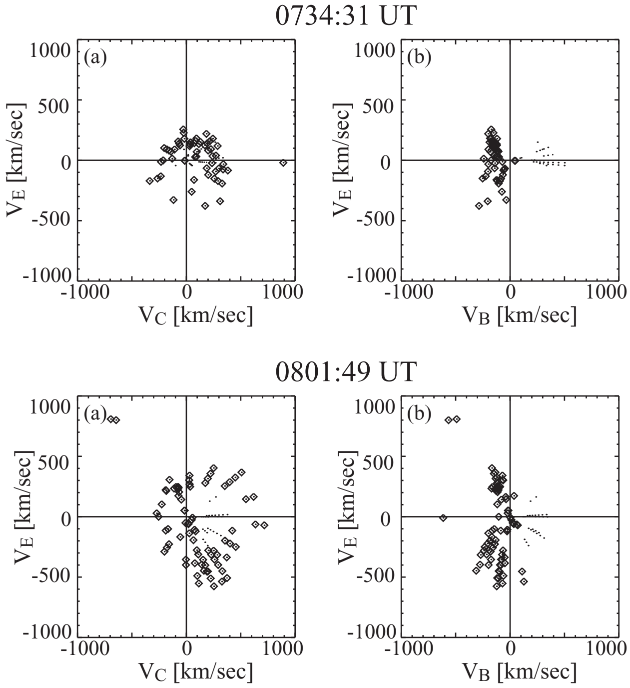

Figure 3.5: Velocity distribution of nonthermal ions observed by the PSA/ISA projected into the plane perpendicular to (a) the magnetic field direction and (b) the convection electric field direction. V_B, V_E, and V_C represent the apparent velocity parallel to the direction of the magnetic field, the convection electric field, and the $E \times B$-drift, respectively. Diamond symbols are the observed velocity of the nonthermal ions and dotted symbols are the observed velocity of the solar wind. Partial ring structures of nonthermal ions are seen in (a).

Section 3.4
Discussion

One of the most important subjects of this study is the issue of the species, sources, and generation mechanisms of nonthermal ions. We discuss these subjects taking the plasma environment near the Moon into account.

3.4.1 Species of Nonthermal Ions

Because the PSA/ISA is an energy-per-charge analyzer, we do not have direct information on the mass and charge of the nonthermal ions. Analyzing the velocity distribution gives us information on the mass and charge of ions. The relationship between the observed and actual velocity of ions is as follows.

$$E_{\text{obs}} = E_{\text{real}}/q = \frac{m_p}{2}\frac{M}{q}v_{\text{real}}^2 = \frac{m_p}{2}v_{\text{obs}}^2, \tag{3.1}$$

so that

$$v_{\text{obs}} = \sqrt{\frac{M}{q}}v_{\text{real}}, \tag{3.2}$$

where m_p is the proton mass, M and q are the mass and charge of the observed ions normalized by those of the proton, E_{real} and v_{real} are the real energy and the real velocity of the observed ions, E_{obs} is the observed energy of the ions, and v_{obs} is the calculated velocity assuming that the observed ions are protons. If these ions are not protons, the observed velocities(v_{obs}) are $\sqrt{M/q}$ times larger than the real velocities(v_{real}).

An example of the M/q-dependence of observed velocity is found in the thermal solar wind shown in Figure 3.3(b). Solar wind is mainly composed of protons($M = 1$ and $q = 1$) and α particles ($M = 4$ and $q = 2$). The PSA/ISA observation can divide them under the condition that they have the same real velocity in the solar wind. Two peaks of the count rate appear at the observed velocity of $\sim$ 350 km/sec and $\sim$ 500 km/sec. The ratio of their observed velocity is $\sqrt{2}$. We interpreted that both the protons and the α particles have a real velocity $v_{\text{real}} \sim 350$ km/sec but the α particles have been observed as if they had a velocity of $v_{\text{obs}} = \sqrt{M/q} \times v_{\text{real}} \sim \sqrt{2} \times 350 \sim 500$km/sec.

We can estimate the mass to charge ratio of the nonthermal ions by their trajectory in the $V_E - V_C$ space. A particle motion in a uniform solar wind is formulated by a simple theory and can be treated as a sum of drift motion and gyration. The drift motion is called $\vec{E} \times \vec{B}$-drift and is independent of mass and charge of ions. When many particles have various gyro-phases, they form a ring in the $V_E - V_C$ space due to the gyration, of

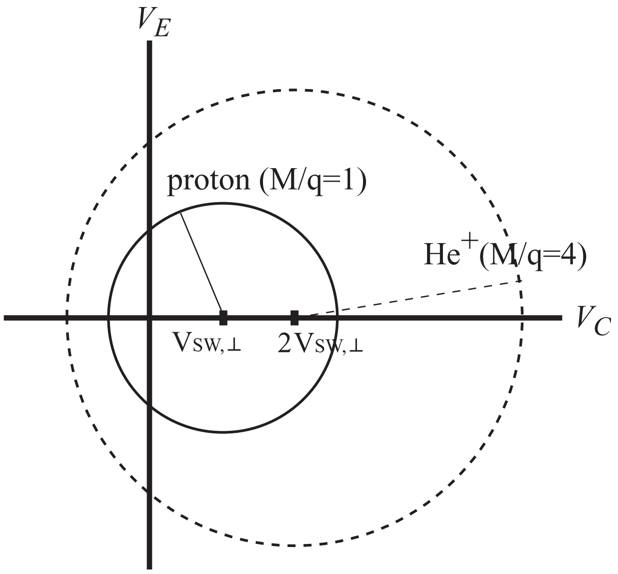

Figure 3.6: Expected trajectory of nonthermal ion in the perpendicular velocity phase space. The solid circle shows the proton trajectory in the velocity space and the broken line shows the He$^+$ trajectory. The circle of the trajectory of particles other than protons is $\sqrt{M/q}$ times larger. Estimating the M/q state is possible by obtaining the center of the ring from the observed ion distribution.

which the center is the $\vec{E} \times \vec{B}$-drift velocity $(V_E, V_C) = (0, V_{\mathrm{SW}\perp})$, where $V_{\mathrm{SW}\perp}$ is a solar wind velocity perpendicular to the magnetic field.

Since the observational data by PSA/ISA contain the information on M/q, the observed velocity is $\sqrt{M/q}$ times larger than the real velocity from equation(3.2). If the observed ions have a different mass or charge from the protons, their $\vec{E} \times \vec{B}$-drift velocity should be $\sqrt{M/q}V_{\mathrm{SW},\perp}$ according to the PSA/ISA as illustrated in Figure 3.6

In Figure 3.7, the estimated values of the $\vec{E} \times \vec{B}$-drift velocities for different numbers of M/q are shown in the phase space plot of nonthermal ions, which is identical to Figure 3.5(a). Solar wind velocities perpendicular to the magnetic field were 139.9 km/sec at 07:34 UT and 245.0 km/sec at 08:01 UT. Determining the center of the ring is difficult because the data deviate strongly at 07:34 UT. The center of the ring seems to locate on the V_C-axis with $M/q < 1$. However, we concluded that the M/q is unity and the species of the nonthermal ions is a proton. The value of M/q is unity because M/q cannot be

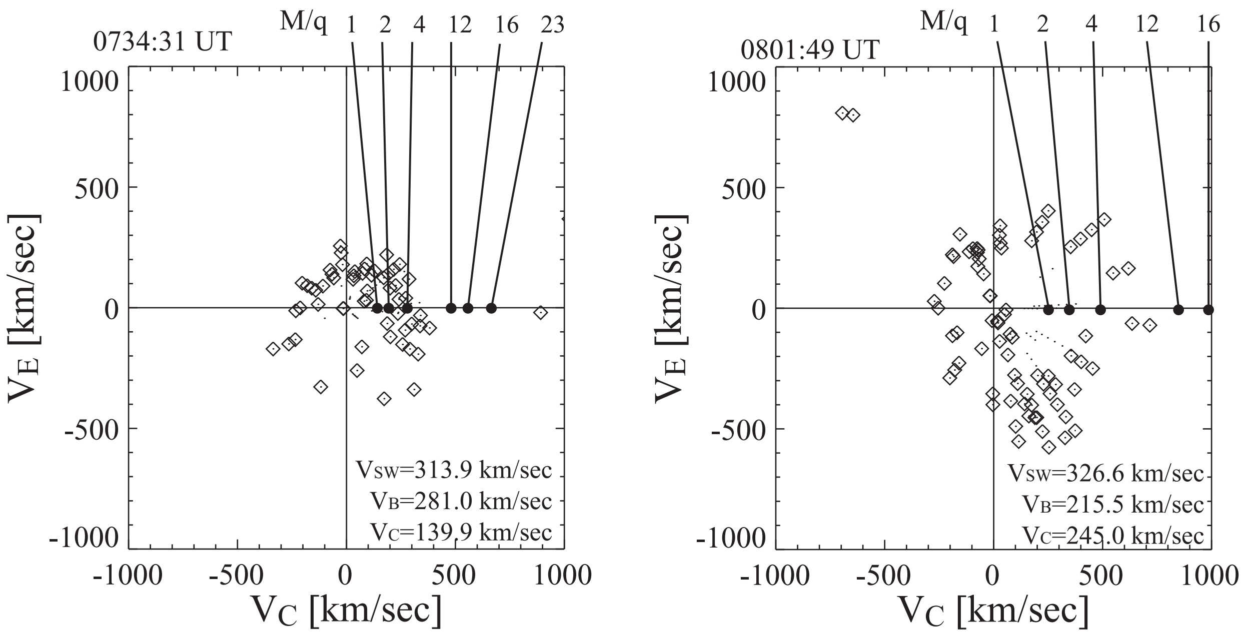

Figure 3.7: Velocity distribution of nonthermal ions observed by the PSA/ISA as in Figure 3.5(a). Drift velocities for different values of $\sqrt{M/q}$ of nonthermal ions are shown.

smaller than 1. We can conclude the species of the nonthermal ions is a proton.

3.4.2 Model Calculation of Nonthermal Ions

Assuming that the nonthermal ions are protons, we traced the trajectories of test particles back in time following the equation of motion as shown below to estimate the source location:

$$\frac{d^2\vec{x}}{dt^2} = \frac{e}{m_p}(\vec{E} + \frac{d\vec{x}}{dt} \times \vec{B}), \tag{3.3}$$

where e and m_p is the proton charge and mass, $\vec{E}$ is the electric field, and $\vec{B}$ is the magnetic field. The calculation started from the satellite location with the velocity observed by PSA/ISA. We assumed a uniform magnetic field of $|\vec{B}| = 3\,\mathrm{nT}$ and a constant solar wind velocity of $|\vec{V}_{\mathrm{SW}}| = 350\,\mathrm{km/sec}$, which are the averaged values during the observation. The magnetic field orientation was estimated from the anisotropy of the electrons, as explained. Further, the convection electric field($\vec{E} = -\vec{V}_{\mathrm{SW}} \times \vec{B}$) was assumed in the calculation.

Figure 3.8 shows the result of calculation, which indicates that most of the ions come from the dayside of the Moon. This implies that the nonthermal ions are generated at or around the dayside of the Moon. The dayside region was the magnetized region of the Moon on that day. Some of the ions look like they do not come from the Moon, but their trajectories pass the lunar surface very closely. The IMF parameters have ambiguities in an amplitude of about 1 nT and in a direction of about 20°, and the plasma waves in the solar wind or in the lunar forewake, such as those observed by *Farrell et al.* [1996], may scatter the ion trajectories.

3.4.3 Initial Velocities of Non-Solar Wind Ions

Knowing the initial velocities of the lunar related ions is vital to specifying the generation mechanism. For example, if the nonthermal ions have zero initial velocity, they might be pickup ions originating from the lunar exosphere because neutral hydrogens in the exosphere have very small thermal velocities.

Figure 3.9 shows the initial velocities of the lunar ions when they are released into interplanetary space. The initial velocities are derived from the model calculation explained in the previous section. The result shows the initial velocities of the lunar ions are close to or larger than those of the solar wind protons. We checked several factors to confirm this conclusion.

First, we checked the ambiguity of the IMF parameters used in our model calculation. We confirmed that the initial velocities had not changed very much after additional model calculations with different but possible magnetic field strengths and directions. We found that the initial velocities should be several hundred km/sec.

Second, we checked the scattering of the ions in the solar wind before they were observed by the spacecraft. Because the magnetometer could not detect waves correctly during the observation, the possibility cannot ruled out observationally. However, the

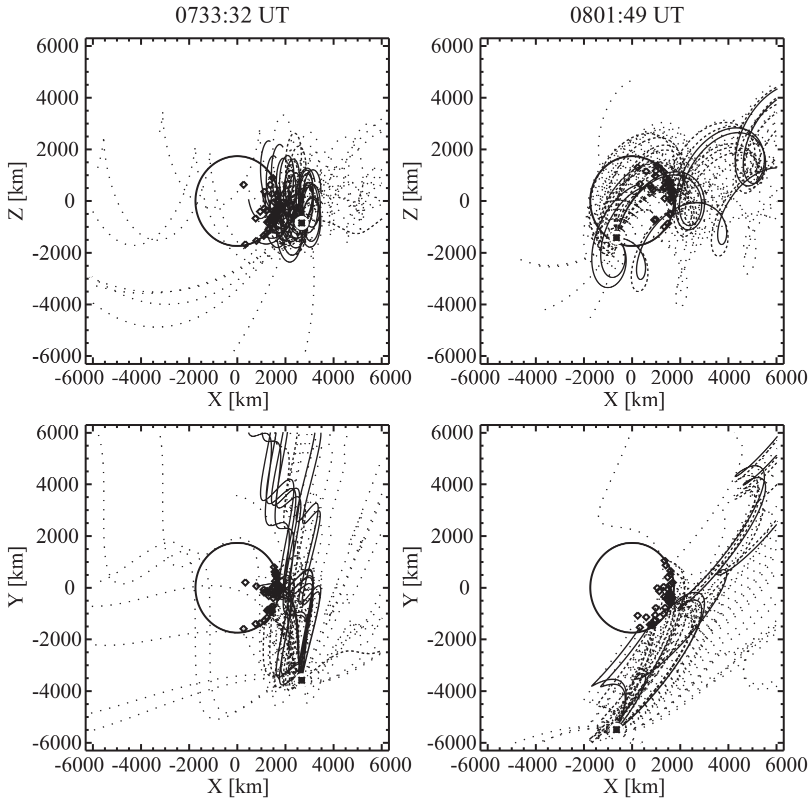

Figure 3.8: Results of model calculation following the equation of motion for observed nonthermal ions at 0733:32 UT and 0801:49 UT. Circles at the center of each figure represent the Moon which is illustrated to scale. The satellite position is shown by black symbols in each panel ((X,Y,Z)=(2670[km], -3580, 690) at 07:33UT and (X,Y,Z)=(-650, -5480, -1420) at 08:01UT). Model calculated trajectory of the incoming protons toward NOZOMI. Solid and dotted lines are the ion trajectories. Trajectories indicated by solid lines have larger counting rates than those indicated by dotted lines. The diamond marks on the lunar surface show the foot location of the nonthermal ions. Most of the ions come from the dayside of the Moon.

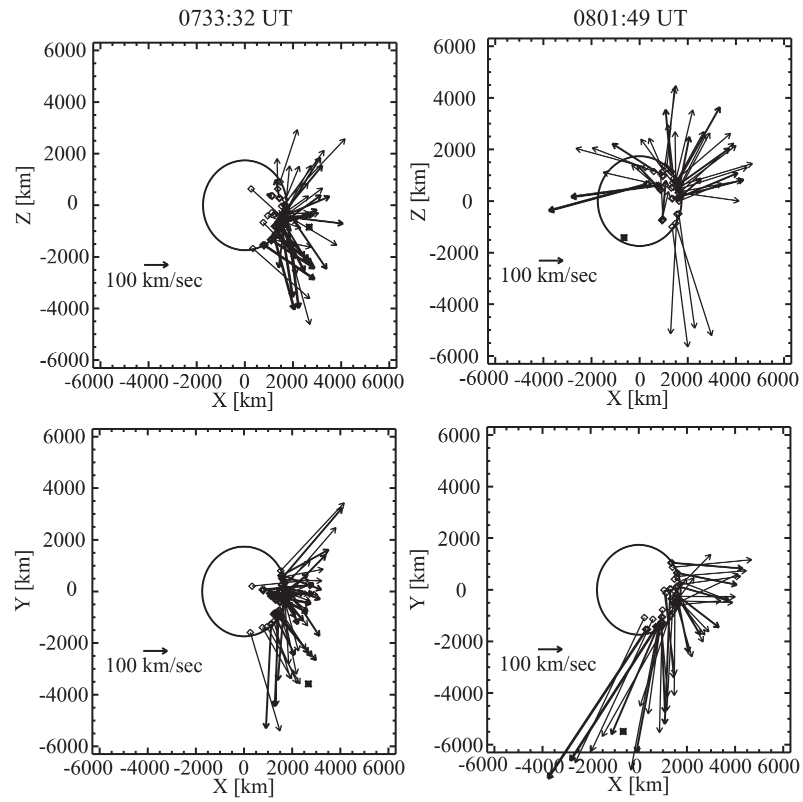

Figure 3.9: Generated locations and initial velocities of the lunar ions at the surface of the Moon. Lunar ions have a large initial velocity comparable to, or larger than, the solar wind protons.

process does not seem feasible. The nonthermal ions only experienced one or two gyro rotations, which is not enough to be scattered. They most likely have large initial velocities.

We also point out that the parallel velocities of the lunar ions in Figure 3.5(b) are several hundred km/sec, which is the same order as or larger than the solar wind velocity. The parallel velocity is opposite to the solar wind parallel velocity. A simple theory that accounts for the ring structure is the collective $\vec{E}\times\vec{B}$-drift. This mechanism only regulates the phenomenon in the plane perpendicular to the magnetic field. The parallel velocity is conserved because no forces parallel to the magnetic field act on the ions.

From those facts, we conclude that the magnitude of the initial velocities should be almost the same as, or larger than, that of the solar wind protons. A large initial velocity is an important clue to discuss the generation mechanism of the nonthermal ions near the Moon as discussed in section 3.4.5.

3.4.4 Relationship With Magnetic Field Direction

Nonthermal ions were detected during the NOZOMI lunar swing-by but they disappeared once between 07:40 and 08:00 UT (see Figures 3.2 and 3.3). One explanation of the disappearance is that the generation of non-thermal ions ceased during this interval. Another idea is that the external electromagnetic conditions changed during the interval. Discussing the first idea is impossible due to the lack of data. We examine the second idea in this section.

Based on the idea of $\vec{E} \times \vec{B}$-drift, a particle with no initial velocity moves in a plane determined by $\vec{V}_{\mathrm{SW}}$ and $\vec{B}$. Small initial thermal velocities parallel to the magnetic field line only cause the particle orbits to slightly deviate from that plane. This means that the nonthermal ions can be only observed under the condition that both the observer and the source location are in or near the plane determined by $\vec{V}_{\mathrm{SW}}$ and $\vec{B}$.

We used a large number of protons for the test particle calculations to verify this idea. When a velocity vector of a test particle at the satellite location is given, the particle can be traced back in time and we can determine whether the particle trajectory has been connected to the lunar dayside or not. A test particle whose trajectory is connected to the lunar dayside could potentially be a lunar related ions. We used 4096 test particles with velocity vectors corresponding to 4096 bins into which the PSA/ISA can divide the velocity space (32 for energy step, 16 for azimuth, and 8 for elevation). A number of ions whose trajectory is connected to the lunar dayside will be obtained among 4096 test particles under given magnetic and electric field conditions. This number is a good parameter for the observation conditions of lunar related ions. We assumed a uniform 3 nT magnetic field, a uniform 350 km/sec solar wind velocity, and a resulting uniform convection electric field. The direction of the magnetic field was varied azimuthally and

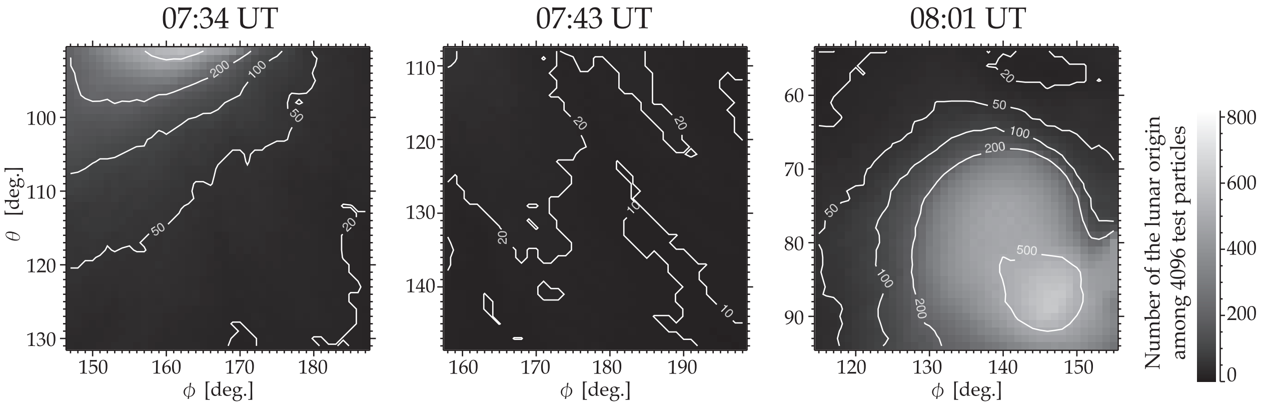

Figure 3.10: Mapping of numbers of the particles that have trajectories connected to the lunar surface, out of 4096 test particles, at 07:34 UT, 07:43 UT and 08:01 UT. The horizontal and vertical axes are azimuthal(ϕ) and elevational(θ) angles of the magnetic field. The center of each panel corresponds to the estimated direction of the magnetic field. Ions from the lunar surface can be observed by NOZOMI under a given solar wind magnetic field condition at 07:34 UT and 08:01 UT, but they cannot be observed at 07:43 UT.

elevationally within $\pm 20^\circ$ around the inferred value to consider the estimation error.

Figure 3.10 shows the result of our calculations. The numbers of test particles whose trajectory was connected to the lunar dayside obtained for 07:34 UT, 07:43 UT and 08:01 UT are shown as a function of the azimuthal and the elevational angles of the magnetic field. It turned out that the nonthermal ions of lunar origin can be observed under the given condition of the solar wind magnetic field at 07:34 UT and 08:01 UT, but they cannot be observed at 07:43 UT even if the 20° estimation error of the magnetic field orientation is considered.

The result of our test particle calculation is consistent with our expectation, and we conclude that the nonthermal ions disappear because of the orientation change of the solar wind magnetic field.

3.4.5 Generation Mechanism of Nonthermal Ions

In this section we discuss possible generation mechanisms of nonthermal ions near the Moon in the following order: 1) solar wind protons deflected by IMF disturbances, independent of the Moon; 2) protons reflected by the Earth's bow shock; 3) heavy ions, which are photoionized or sputtered by the solar wind or by micrometeorites, escaped from the surface of the Moon; 4) protons or heavy ions ionized by photoionization, charge exchange; or energetic electron impact in the lunar exosphere; and 5) solar wind protons deflected in the vicinity of the Moon.

The first mechanism can be readily ruled out because the nonthermal ions only emerged when the satellite was very close to the Moon, and the result of the model calculation (Figure 3.8) tells us that the source is the Moon.

The second mechanism can be ruled out even if this mechanism seems to be the most plausible at first glance. Some protons injected into the Earth's shock is reflected by the shock potential at the front, and are reflected back to the upstream region(*Thomsen* [1985]). When they reach the NOZOMI, they must have a ring structure in the velocity phase space. However, this mechanism is not realized because the model calculation shows that the source regions are not the Earth even if the $20°$ error of the magnetic field estimation is considered.

The third mechanism is based on the idea that lunar material is ejected out to the interplanetary space. *Hinchenbach et al.* [1991] and *Mall et al.* [1998] observed such a component in the downstream of the Moon. However, this mechanism can also be ruled out because the observed M/q is too small in our case.

The fourth mechanism is an analogy of the pickup ions near comets, Venus and Mars. Our analysis of the M/q state shows that the species of nonthermal ions is proton. When neutral hydrogens are ionized in the dayside of the Moon, the initial velocities of the generated protons must be very small. This contradicts our observations. One may say that the small magnetized regions on the surface of the Moon create perturbation in the solar wind and generate electromagnetic waves that accelerate the ionized protons at a low altitude. If this is the case, very thin layer near the Moon must have an effective acceleration mechanism. This also does not seem feasible.

The fifth mechanism is the most plausible mechanism for interpreting our observation, because it can explain the M/q state and the large initial velocity of the ions. The Moon has neither a global magnetosphere nor bow shock. This means that global-scale electromagnetic disturbances cannot be created around the Moon and, consequently, they cannot act as an ion deflector. One possible candidate for the deflector is the floating potential of the Moon body embedded in the solar wind. Another candidate are the small-scale magnetic field anomalies distributed on the surface of the Moon or some mechanisms related to the anomalies. We further discuss this mechanism in the next section.

3.4.6 Proton Deflector in Front of Moon

When the solar wind ions are deflected preserving the first adiabatic invariant such as formed in the mirror reflection, the reflected ions have a twostream beam structure in the velocity space. The beam instability increases the occupancy of the reflected ions in the velocity space and the reflected ions form a shell-like structure. This mechanism cannot explain our observation of the partial ring structure. The deflection mechanism near the Moon must destroy the first adiabatic invariant so that some dynamic structure must exist in the vicinity of the Moon. Electrostatic potential, which is produced by the photoelectron layer on the lunar surface, could be one of the candidates. However, it is reported that the potential has been reported to reach approximately 10 volts at most (*Benson et al.* [1975]), so it cannot deflect the solar wind protons with energies of about 1 keV.

Another possibility is a nonuniform magnetic field structure near the Moon surface. The Moon has some anomalous magnetic fields with horizontal scales of 100$\sim$1000 km, which is comparable to, or larger than, the solar wind proton gyro radius($\sim$80 km during the observation).

Stochastic deflection due to the finite Larmor radius effect around the magnetic anomaly can be considered, but explaining the observed protons with a larger initial velocity than that of the solar wind.

The miniature bow shock around the anomalous magnetic field proposed by *Lin et al.* [1998] and *Harnett and Winglee* [2000] is also another possible candidate and it is the most suitable for interpreting the observation. It can explain the protons with a large initial velocity in the upstream region of the collisionless shock (for example, *Paschmann et al.* [1981]; *Thomsen* [1985]). Large magnetic anomalies on 1000-km scales are distributed on the farside of the Moon so that the interaction between the anomaly and the solar wind is the most effective during the observation when the moon phase is new moon.

We suggest that deflection mechanism of the miniature bow shock is due to the interaction between the lunar crustal magnetic anomalies and the solar wind, but NOZOMI's observation is very limited in space and time, so the problem of the proton deflection mechanism remains unsolved. To understand the deflection mechanism, we should observe the height profile of the 3-D velocity distribution functions and the spatial distribution of the nonthermal ions.

Section 3.5
Summary

Having analyzed the 3-D distribution functions of ions obtained in the vicinity of the Moon, we found that protons are injected into the interplanetary space from the Moon with fluxes of $10^6 \sim 10^7$/ cm^2 sec. Their source is the dayside region of the Moon, where the magnetic anomalies was mainly distributed during the observation. They are observed only under the specific condition of the solar wind and the spacecraft location relative to the Moon body. They have large initial velocities comparable to, or larger than, those of the solar wind and have the velocity distribution function of a partial ring structure.

Based on these results and our discussion, we propose the following scenario for lunar ions: the vicinity of the Moon must have a deflector which deflect a part of the solar wind protons around the lunar surface while most protons are absorbed when they reach the lunar surface. The miniature bow shock, resulting from the interaction between the lunar magnetic anomalies and the solar wind, is the most likely candidate. Note that the first adiabatic invariant is broken during the deflection. The deflected protons have large velocities due to the bulk velocity of the solar wind, and they move under the force exerted by the convection electric field and gyrate around the magnetic field in the solar wind. This motion forms a partial ring structure with large initial velocities in the velocity phase space as observed by the PSA/ISA. The observation of nonthermal ions proves that a dynamic electromagnetic structure exists in front of the Moon.

Lunar ions are important for studying the plasma environment near the Moon. But the data was not sufficient to comprehensively understand the physics of the lunar ions, especially the deflection mechanism of the solar wind. We will continue model calculations to investigate the deflection mechanism and estimate the deviation of the trajectory of the lunar ions. We also suggest global in situ observations of the 3-D velocity distribution functions to study the acceleration mechanism. In addition, we suggest observing the lunar ions from a distance of several lunar radii in various electromagnetic environments, various $F_{10.7}$ parameters, moon phases or for different amounts of micrometeorites. These observations will enable us to completely understand the generation mechanisms and the diffusion processes of lunar ions. Understanding these mechanisms also enhances our knowledge on pickup ions around unmagnetized bodies, like comets, Mars and Venus.

Chapter 4
Electric Potential in the Lunar Wake

Section 4.1
Introduction

4.1.1 Solar Wind Electrons

The solar wind electrons have three components; core, halo and strahl. The thermal component is called core. The typical temperature of the core is 10-20 eV, which corresponds to velocities of ∼1800-2500 km/s. The thermal velocity of the solar wind electrons is larger than the bulk velocity.

One of the suprathermal components is called the halo component. Its typical temperature is 60-100 eV. Because the corresponding velocities (4500 km/s for 60 eV) are much larger than the bulk velocity, the bulk velocity can be ignored.

The strahl component, of which typical energy is 100∼1000 eV, is a narrow beam extended along the magnetic field line and the flux moving away from the sun is larger than that moving toward the sun. When the nominal strahl electrons are observed in the specific energies, it looks as if the electrons were flowing away from the sun along the magnetic field.

Sometimes, the electrons flowing toward the sun are enhanced. The electron velocity distributions in this case is called "counterstreaming electron distribution." Such a distribution is realized when both ends of the magnetic field line are connected to the sun, the interplanetary magnetic field lines form loop-like structure, and the interplanetary magnetic field lines are connected to the Earth's bow shock.

4.1.2 Electrons in Relation to Moon

Very little observations on the electrons were conducted in the vicinity of the Moon, especially using the modern instruments. It is known that the Moon has tenuous ionosphere as described in Section 1.2.1. The ionospheric electrons are photoelectrons in the dayside of the Moon. Apollo observations detected such photoelectron-layer (see review by *Stern* [1999] and references therein).

Lin et al. [1998] reported the electron spectra observed by LP. They reported the enhancement of electron flux and the coincident whistler activity near the magnetic anomaly. These detections are the direct evidence for the presence of a shock wave around the lunar magnetic anomaly.

Counterstreaming electrons are reported by WIND observations in the forewake region of the Moon (*Farrell et al.* [1996]). They reported the simultaneous detection of ULF wave activities and counterstreaming electrons, and concluded that the ULF waves are formed by the counterstreaming electrons which may be reflected by the ambipolar potential.

The amplitude of the ambipolar potential is discussed in *Ogilvie et al.* [1996]. They used solar wind ion data which was accelerated by the ambipolar potential and concluded that the amplitude was 400V. The value is extremely large compared with numerical simulations. *Birch and Chapman* [2001] simulated the void region formed behind the Moon by particle simulations and concluded that the ambipolar potential was $\sim$40V.

In this chapter, the plasma environment in the vicinity of the Moon are discussed using electron velocity distribution functions observed by NOZOMI spacecraft. Counterstreaming electrons are found during its lunar swing-by. By the analyses of the electron spectra, it is revealed that the backstreaming electrons are from the lunar wake. The backstreaming electrons are thought to contain informations on the lunar wake.

Section 4.2
Instrumentation

Observations of the 3-D electron velocity distribution functions were performed with the Particle Spectrum Analyzer/Electron Spectrum Analyzer (PSA/ESA) mounted on the NOZOMI spacecraft. The PSA/ESA can measure electrons from 12 eV to 15 keV in 32 energy steps. With one spin rotation (about 6.5 s during the lunar swing-by), the PSA/ESA could cover a full 4π sr viewing angle with 22.5×22.5 angular resolution. Because of telemetry limitations, approximately 1/10 of the data (about 1-min period) were transmitted until 0737 UT, and no data could be obtained from 0719 UT to 0724 UT and from 0737 UT to 0742 UT. Between 0742 UT and 0747 UT, all spin data were obtained. More detailed characteristics of the PSA/ESA can be found in a paper by *Machida et al.* [1998].

The energy range of ESA was set to be between 12 eV and 3 keV during the lunar swing-by of NOZOMI. The electron data with energies less than 60∼80 eV were contaminated by various non-solar-wind electrons. They may be photoelectrons generated at the surface of the spacecraft. Because it was difficult to eliminate the photoelectrons, the electron data with energy range less than 80 eV were not used in the analysis.

Information on the magnetic field are important for analyses of electron data. To understand the electron kinetics, the orientation of the magnetic field is necessary. Because of the lack of the magnetic field data during the lunar swing-by, the estimated magnetic field orientation was used in this chapter. The estimation error is less than 27° as described in Chapter 2.

Section 4.3
Observations

4.3.1 Electron Flux During Lunar Swingby

During the NOZOMI's lunar swing-by on Dec. 18, 1998, PSA/ESA successfully observed 3-D electron velocity distribution functions. The closest approach was at 0734 UT with an altitude of 2,800 km above the lunar surface. The trajectory of NOZOMI is drawn in Figure 3.1.

Figure 4.1 displays electron differential flux observed by ESA during the NOZOMI swing-by. The top panel shows the omnidirectional differential flux of the electrons with energies of 89, 160, 293 and 527 eV. The open circles are the observational data by ESA and the solid lines show the averaged flux of the interval between 0708 UT and 0716 UT, when the electrons were not disturbed by the Moon.

The remaining three panels show the differential flux of the electrons with pitch angles (α) of $0° < \alpha < 30°$, $75° < \alpha < 105°$ and $150° < \alpha < 180°$. The IMF was pointing away from the sun during the lunar swing-by, so that the electrons with zero pitch angle were flowing away from the sun along the magnetic field, and those with the pitch angle of 180° were flowing toward the sun.

The nominal flux of the electrons moving away from the sun ($\alpha < 30°$) is larger than that moving toward the sun ($\alpha > 150°$) in Figure 4.1. The characteristics of the electron flux do not contradict previous observations in the solar wind.

When NOZOMI approached to the Moon, the flux of the backstreaming electrons were enhanced to the level of that of strahl electrons, namely, counterstreaming electrons were observed in the vicinity of the Moon. On the other hand, the flux of the solar wind did not change.

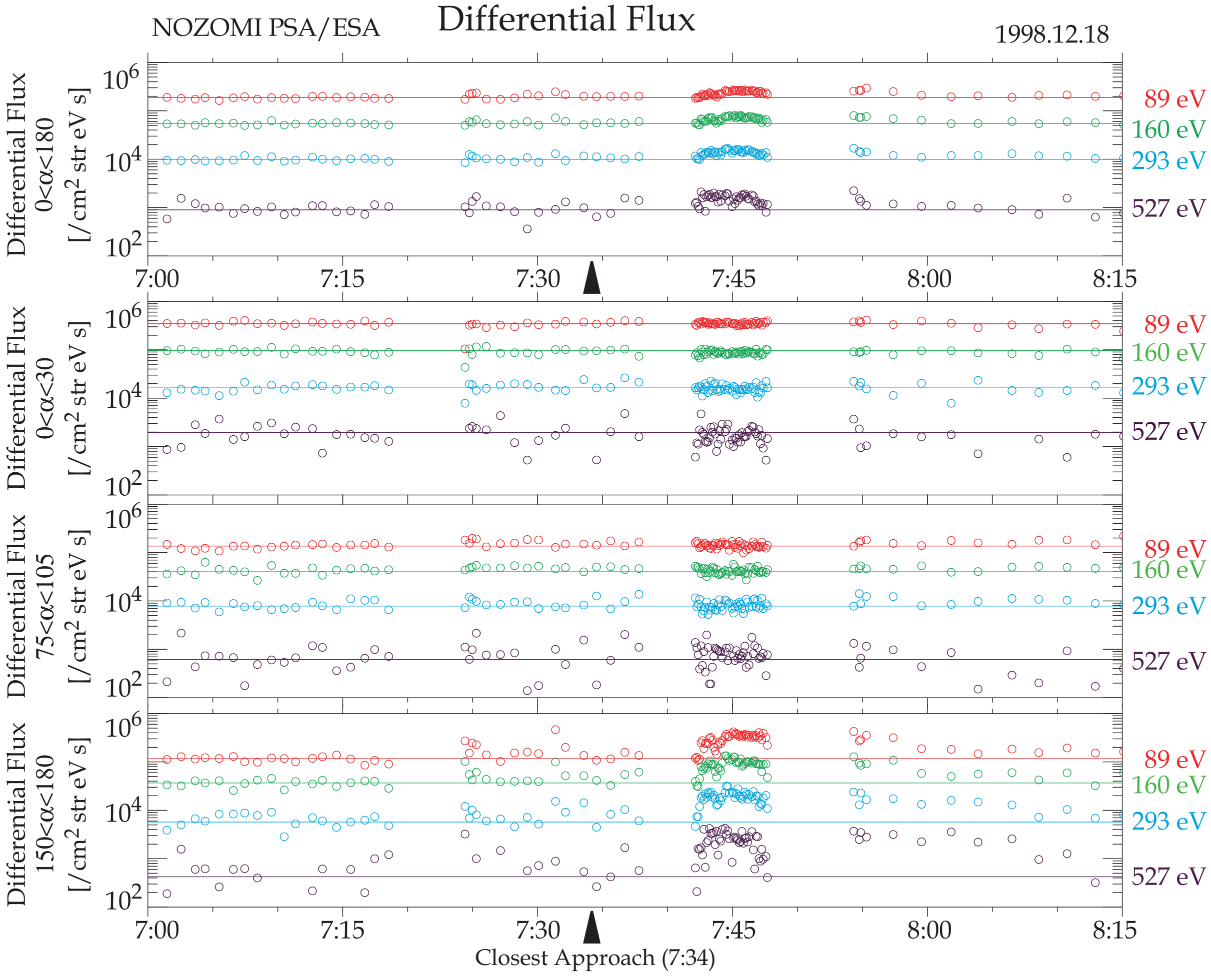

Figure 4.1: Observed differential flux of the electrons during the lunar swing-by. The top panel shows the omnidirectional differential flux with energies of 89, 160, 293 and 527 eV. Open circles indicate the observational data by ESA. Solid lines are the nominal level of the solar wind electrons calculated by the data between 0708 and 0716 UT. The remaining panels are the differential flux of electrons with pitch angle of $0° < \alpha < 30°$, $75° < \alpha < 105°$ and $150° < \alpha < 180°$. When NOZOMI was close to the Moon, the backstreaming electrons ($150° < \alpha < 180°$) were enhanced.

During the lunar swing-by, the solar wind was very stable as shown in Figure 3.2 in Chapter 3, so that the enhancement is thought to be related to the Moon. In the followings, the characteristics of the counterstreaming electrons are discussed using 3-D velocity distribution functions.

4.3.2 Characteristics of Counterstreaming Electrons

Detailed characteristics of the electron distribution functions observed in the vicinity of the Moon are discussed in the followings. The electron data are separated into three intervals; during 0708 UT and 0716 UT (solar wind for reference), 0725 UT and 0736 UT (event 1), and 0742 UT and 0743 UT (event 2). All intervals contain 8 spins. The data used in the analyses are the averaged value over 8 spins.

The electron data obtained in the normal solar wind during 0708 UT and 0716 UT are shown in Figure 4.2. Four left panels in Figure 4.2 show the full two-dimensional angular distribution of electrons with energies of 358, 239, 160 and 108 eV, observed during 0708 UT and 0716 UT (top panels) and the pitch-angle-sorted electron counts with the same energy steps (bottom panels). Here we used a spacecraft coordinate (SC) system, which has the origin at the spacecraft center and the z axis parallel to the spin axis. The x-axis is perpendicular to the z-axis and lying on a plane that contains the z-axis and the sun. The y-axis is defined so as to form the right-hand system. In the upper panels, the direction of zero spin angle is defined to contain the sunward flow vector of the electrons. The orientation of the averaged magnetic field (i.e., the elevational angle θ and the spin angle ϕ of the magnetic field) was determined as being $\theta = 152°$ and $\phi = 149°$ in the SC coordinate system, which corresponds to the components of the unit vector of the magnetic field to be (-0.85, 0.37, -0.36) in the GSE as well as LCGSE coordinate systems. Pitch angle ($\alpha = \tan^{-1}(v_\perp / v_\parallel)$) contours of 30°, 60°, 90°, 120° and 150° with respect to the estimated magnetic field orientation are also superimposed on the electron angular distribution data. Using the estimated magnetic field orientation, we obtained the electron

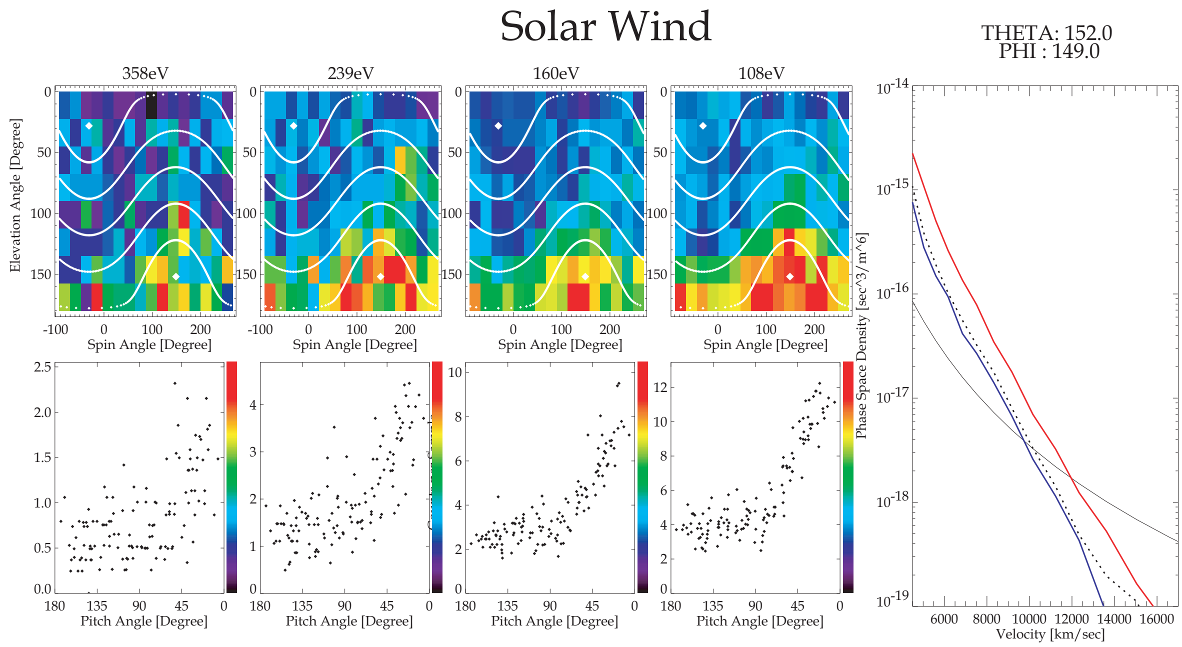

Figure 4.2: Detailed electron data obtained at 0708-0716 UT, when normal solar wind electrons were detected. The data are averaged over eight spins. The four left panels show (top) the angular distribution of electrons and (bottom) the pitch-angle-sorted electron counts with energies of 358, 239, 160 and 108 eV. The curves in the upper panels indicate the pitch angle contours of 30°, 60°, 90°, 120° and 150° with respect to the estimated magnetic field. The right panel shows the velocity distribution functions of electrons. The red curve is for the antisunward flowing electrons, the blue curve is for the sunward streaming electrons, and the dotted curve is for the electrons having velocities perpendicular to the magnetic field. The thin solid curve is the one-count level of PSA/ESA.

pitch angle distribution; the results are shown in the lower panels. The right panel in Figure 4.2 displays the velocity distribution functions of electrons. The red curve is for the electrons with pitch angle of $0° < \alpha < 30°$, which stream away from the sun along the magnetic field, and the blue curve is for those of $150° < \alpha < 180°$, and which stream toward the sun along the magnetic field, the dotted line is for those of $90° < \alpha < 120°$, which have velocities perpendicular to the magnetic field line that are trapped by the magnetic field. The thin black curve shows the one-count level of PSA/ESA. As can be seen, these data had a common solar wind character in that the phase space density of electrons away from the sun was 5 times larger than that toward the sun, and both had

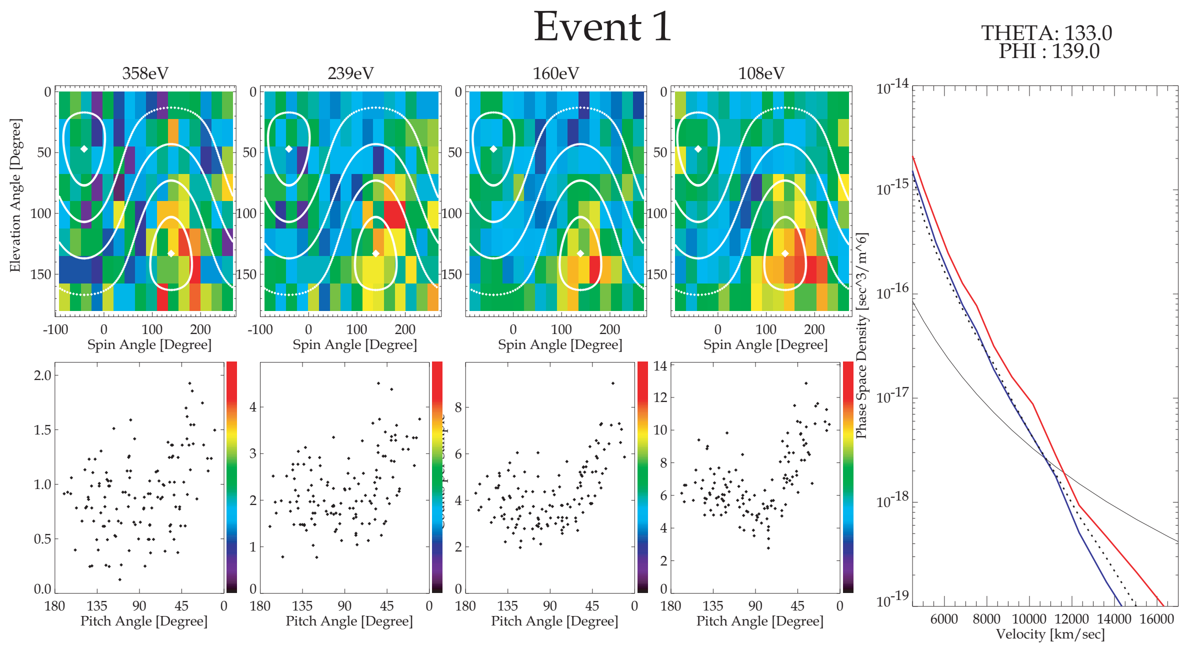

Figure 4.3: Detailed electron data at the time of event 1 occurred (0724 UT-0736 UT), in the same format as Figure 4.2. Data are summed over eight spins. Compared with Figure 4.2, there are more electrons with pitch angle $\alpha > 90°$, which implies the counterstreaming distribution.

power law distributions for velocities over ~7000 km/s.

The observational result around 0730 UT when the first enhancement of electron counts was observed is shown in Figure 4.3 in the same format as Figure 4.2. The data in Figure 4.3 are also eight-spin-period data. Because of the low edit rate of NOZOMI, we could not sum over a continuous time interval so that we used data when backstreaming electron flux were apparently enhanced (Figure 4.1). The magnetic field, which was also estimated from the three-dimensional electron velocity distribution function, was $\theta = 133°$ and $\phi = 139°$ in the SC coordinate system (the unit vector of the magnetic field had components of (-0.86, 0.52, -0.04) in the GSE and LCGSE coordinate systems) and was slightly different from the previous case in the solar wind. It is obvious that the backstreaming electrons along the magnetic field were broadly enhanced in the color-coded angular distribution maps of Figure 4.3. This can also be clearly seen in the lower

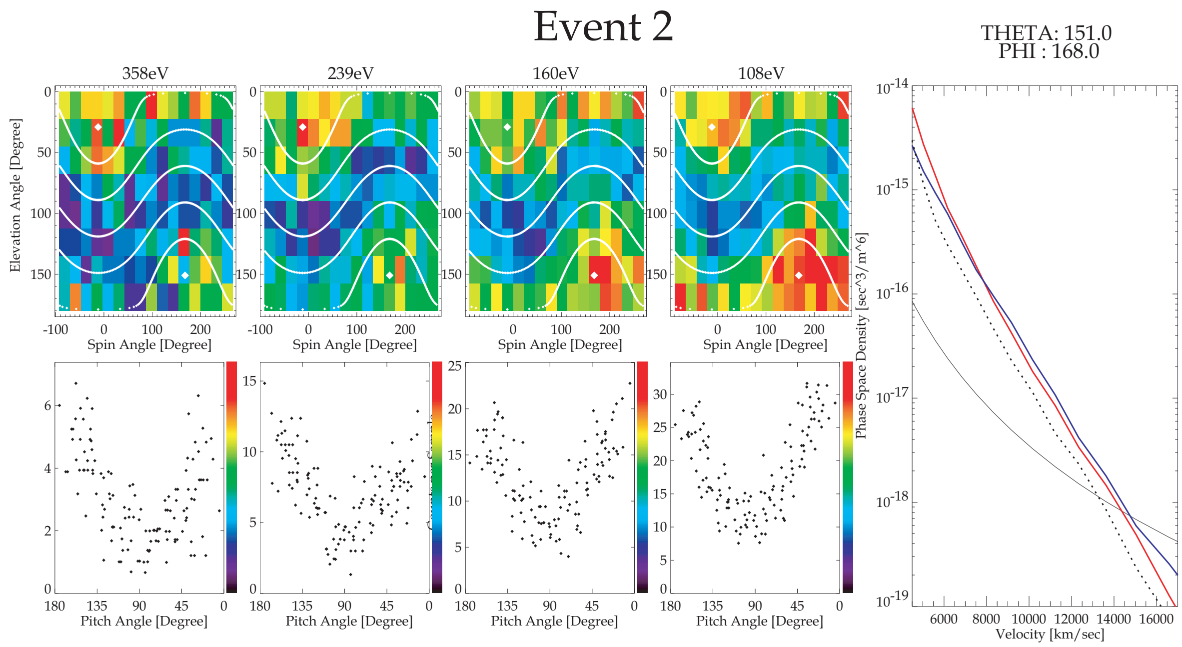

Figure 4.4: Detailed electron data at the time event 2 was observed (0742 UT-0743 UT). The format is the same as Figure 4.2. Data are summed for eight spins. In this case, the backstreaming electrons seem to be thermalized.

four panels of the pitch angle count data; namely, electron counts with pitch angles of more than 90° were clearly enhanced.

Figure 4.4 shows the observational results at ∼0743 UT, when the second electron flux enhancement occurred. The features of electrons look similar to event 1, but there are some differences from that event. One of the most important differences is that there was no significant flux decrease around 180° pitch angle. The second difference is that the reflected electrons have comparable flux to the ambient solar wind electrons or they dominate the ambient solar wind electrons in the higher energy ranges. This can be clearly seen in the velocity distribution functions. Namely, the backstreaming reflected electrons ($150° < \alpha < 180°$) overwhelm the nominal electrons ($0° < \alpha < 30°$) at higher energies, i.e., in the higher velocity range ($\gtrsim$8000 km/s). This implies some mechanism that thermalized the solar wind electrons and reflected them back along the magnetic field line to the spacecraft location.

Similar events of backstreaming electron enhancement were observed during the time interval from 0745 to 0755 UT. Their characteristics are the same as event 2.

Since the signatures of the electron distribution functions are different in event 1 and event 2, it is appropriate to assume that the reflection processes are different for these two cases. We discuss the reflection process in the following section.

Section 4.4
Discussion

4.4.1 Location of Electron Reflection

It is essential to determine the location where the electron reflection occurred to understand the mechanism of the reflection. Since the electrons in the energy range over 80 eV, which are studied in this chapter, had velocities much faster than the bulk velocity of solar wind electrons, we can roughly consider that the enhanced electrons simply came back along the magnetic field line.

The locations of the Earth, Moon, and NOZOMI and the magnetic field which crossed the spacecraft and the solar wind ion velocity at 0711:22 UT, when no reflection events were observed, are shown in Figure 4.5. In each panel, the thick line corresponds to the magnetic field, and the arrow almost along the $-x$ direction indicates the solar wind ion velocity. The dotted line is a trajectory of the Moon (right panels) and NOZOMI (left panels). The left and right panels are shown in the GSE and LCGSE coordinate systems, respectively. The orientation of the magnetic field was also obtained from the electron data.

Figure 4.6 shows the results at 0732:08 UT, when event 1 occurred, in the same format as Figure 4.5. The magnetic field pointed toward the nightside region in the vicinity of the Moon, namely, the lunar wake region.

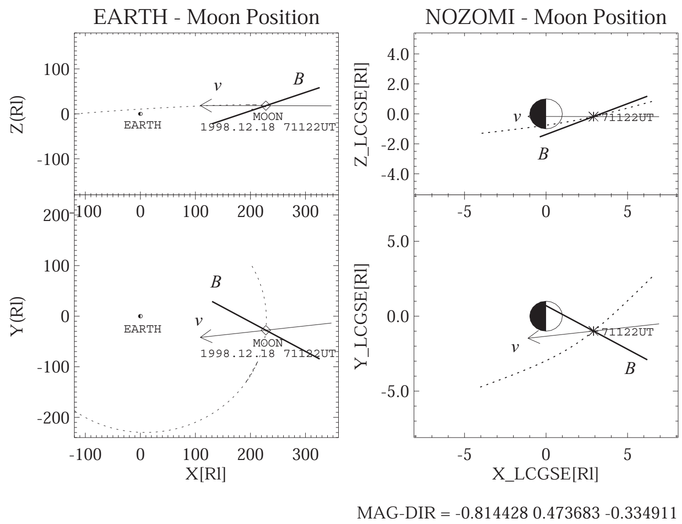

Figure 4.5: Locations of Earth, Moon, and NOZOMI at around 0711:22 UT, when the nominal solar wind was observed. The LCGSE coordinate systems are used. The solid thick line in each panel shows the estimated magnetic field orientation, and the arrow shows the direction of the solar wind

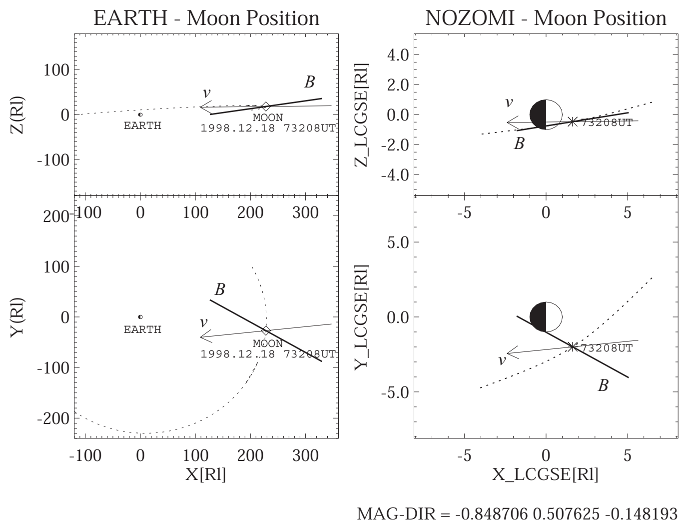

Figure 4.6: Locations of the Earth, Moon and NOZOMI at the time event 1 occurred, (0732:08 UT). The format is the same as in Figure 4.5. The magnetic field pointed toward the lunar wake region in this case.

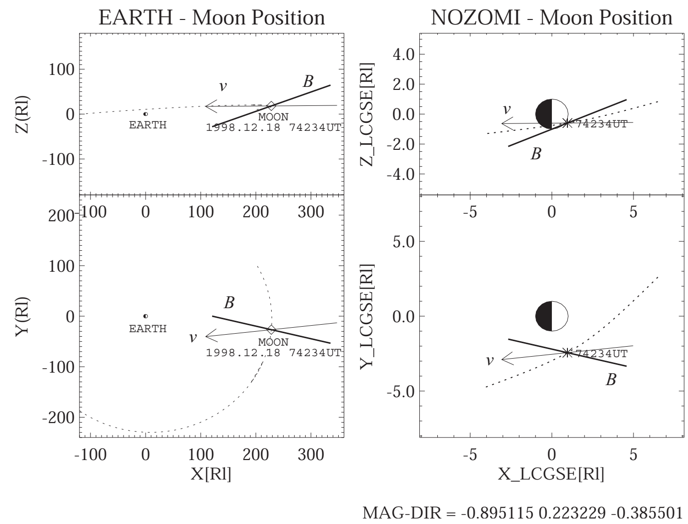

Figure 4.7: Locations of the Earth, Moon and NOZOMI at the time of event 2 (0742:34 UT). The format is the same as in Figure 4.5. The magnetic field did not seem to reach the lunar wake region.

Figure 4.7 shows the results for event 2. In this case, the magnetic field line did not seem to traverse the lunar wake region. However, taking $\sim 20°$ error of the magnetic field orientations into consideration, it is possible to conclude that the magnetic field is connected to the lunar downstream region, where the two-stream instabilities develop.

The above discussions on magnetic field observation revealed that the downstream structures of the Moon are very important for the reflection of the counterstreaming electrons.

4.4.2 Reflection Mechanism on Event 1

The characteristics of the plasma and the magnetic field in the lunar wake region have been discussed since the late 1960s. Solar wind plasma particles collide with the lunar surface and are simply absorbed, creating a void region in the downtail. The plasma passing the terminator flows into the void region, and rarefaction waves are created simultaneously. In the void region the magnetic field is intense in order to maintain the pressure balance

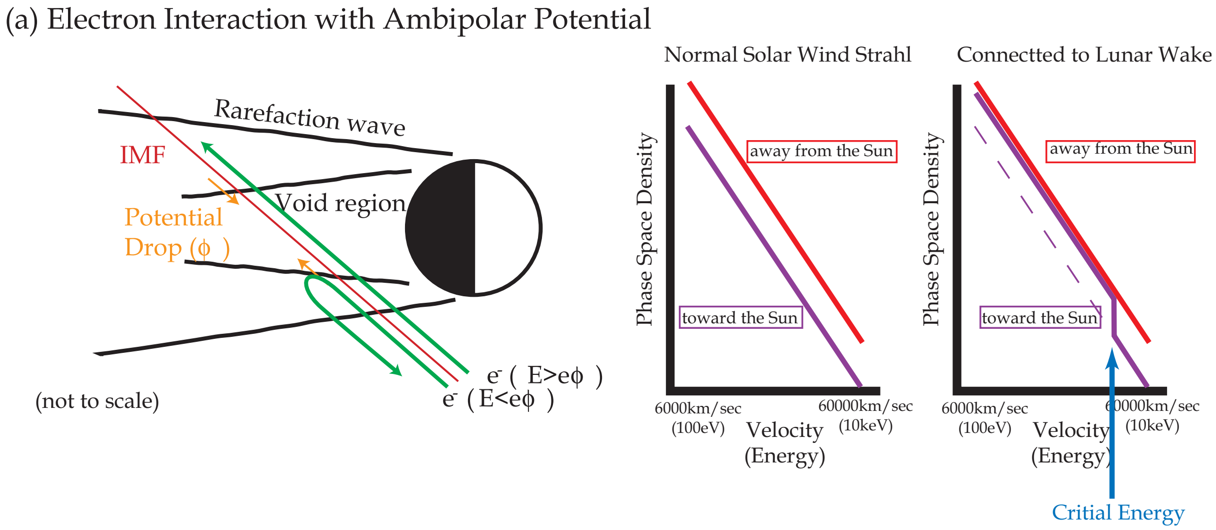

Figure 4.8: Illustration of the electron reflection by ambipolar potential drop. (Left panel) Electrons with energies larger than the electrostatic potential can travel through the wake. Electrons with lower energies are reflected back by the potential. (Right panels) The index of the backstreaming electron spectrum is unchanged because the reflection do not change the energy of the electrons. There is a critical energy corresponding to the potential drop.

with the solar wind (*Michel* [1968]).

Recently, plasma measurement in the lunar wake has been conducted, and it was reported that the ions were accelerated along the magnetic field line by ambipolar diffusion process (*Ogilvie et al.* [1996]). This process was comprehensively shown by computer simulation (*Farrell et al.* [1998]). The ambipolar electric field accelerates the ion in the direction of the plasma expansion, but it also reflects the electrons in the opposite direction. Those electrons can escape the wake region along the magnetic field line and form the counterstreaming electron distribution in the vicinity of the Moon. This can be a possible mechanism to account for event 1.

According to this mechanism, an electron with kinetic energy greater than that which corresponds to the potential drop cannot be reflected back and travel through the wake (Figure 4.8). Therefore we have no reflected electrons in a higher energy range. As can be seen in Figure 4.3, there are backstreaming antisunward electrons in event 1 in the velocity range below 8000 km/s, compared with the solar wind case which is shown in Figure 4.2. The ratio of the phase space densities for sunward, trapped, and antisunward electrons seems to take about the same value to the nominal solar wind case beyond 13,000 km/s. This corresponds to a 480V potential drop, which is close to the value of 400 V obtained by *Ogilvie et al.* [1996] on the basis of accelerated ion data from the WIND spacecraft.

However, the value of 480V is too large compared to the results of 40V by the particle calculation (*Birch and Chapman* [2001]). This may result from some assumptions in the calculation model. The mass ratio of 20 in the calculation is too small to realize the ambipolar diffusion because the mechanism largely depends on the difference of thermal velocity between the solar wind ions and electrons. The nonthermal electrons which are often ignored by the numerical calculation also control the actual physics of the ambipolar diffusion.

Other possible mechanisms of the generation of the counterstreaming electrons should be argued. One possibility is that backstreaming electrons resulted from the magnetic mirror effect of the lunar crustal field. This idea is compatible with the reduction of the electron flux near 180° pitch angle, which indicates the existence of a loss cone as can be seen in Figure 4.3. From the observations of Apollo Subsatellite and the Lunar Prospector, we know that there are regions on the lunar surface that are characterized by crustal magnetic fields. If the solar wind magnetic field were connected to the magnetized crustal region and this intensified the magnetic field, then the electrons with small pitch angles would be reflected by the mirror force and return along the magnetic field line. This mechanism could produce similar characteristics in the electron data as event 1.

However, there is a difficulty; namely, the solar wind magnetic field cannot be connected to a spatially confined magnetized crustal region, whose scale size is very small, for at least 6.5 s (one spin period of NOZOMI). The idea of a miniature bow shock is related to this mechanism. According to *Lin et al.* [1998], a miniature bow shock can be generated in front of the crustal magnetic field anomaly region. However, this possibility is also excluded for the same reason as the mirror force due to the crustal magnetic field;

namely, the miniature bow shock is too small to be connected for at least 6.5 s by the magnetic field. Moreover, the nonthermalized velocity distribution in event 1 also negates this model.

The mirror force by the magnetic field enhancement inside the void regions can reflect the electrons. The critical pitch angle of the mirror reflection (α_c) can be calculated by simple theory;

$$\frac{B_i}{\sin^2 \alpha_c} = B_m, \tag{4.1}$$

where B_i and B_m are magnetic field intensity in the interplanetary medium and umbral region, respectively. The ratio of the magnetic field strength (B_m/B_i) is about 1.25 (*Whang and Ness* [1972]) so that the critical pitch angle is α_c =63°, namely, solar wind electrons with pitch angle less than 63° will not be reflected. The observed pitch angle distributions in Figure 4.3 contradicts the above inspection.

The combined effect of the potential drop associated with the ambipolar diffusion and the mirror reflection due to the magnetic field enhancement in the lunar wake is also the other mechanism. Although the loss cone angle observed by NOZOMI seems to be too small, the loss cone angle can apparently decrease when the reflected electrons fill the loss cone considerably. Therefore, the mechanism should be considered with the non-fluid approach, and it may explain the decrease of the reflected electrons in the velocity component parallel to the magnetic field.

A further possibility for the source of the backstreaming electrons is photoelectrons generated in the tenuous lunar ionosphere or at the lunar surface. In event 1 (0724-0736 UT) the magnetic field can be said to point to the lunar surface when deviations of the estimated magnetic field are considered. If this configuration really occurred, the photoelectrons could have traveled along the magnetic field to the spacecraft's location. However, the spectrum of the backstreaming electrons of event 1 (the blue curve in the right panel in Figure 4.3) is very similar to that of the solar wind (that in Figure 4.2). It is natural to think the backstreaming electrons are the solar wind electrons reflected by electrostatic potential.

4.4.3 Reflection Mechanism on Event 2

As for event 2, we cannot conclude that the reflection process is due to the ambipolar potential drop in the lunar wake for two reasons. First, the magnetic field did not seem to point toward the lunar wake region, as can be seen in Figure 4.7. Second, the back-streaming electrons were thermalized differently from event 1. The thermalized spectrum of the backstreaming electrons denies the mirror reflection of the solar wind electrons as explained in the previous section. The ionosphere originated electrons are also ruled out because the magnetic field did not point to the lunar surface.

Another possibility is that these counterstreaming electrons are created in the interplanetary shock. However, as can be seen in Figure 3.2, which indicates the magnetic field obtained by the electron data in the GSE coordinate system, no dynamic change in the magnetic field occurred around the time this event was observed. Moreover, interplanetary shocks have a smaller Mach number than the bow shock. Consequently, perpendicular heating is stronger than parallel heating (*Feldman et al.* [1983b]). Our observational results do not exhibit notable perpendicular heating (Figure 4.2 and Figure 4.4).

An alternative interpretation of this event is that the reflected electrons originated from the terrestrial bow shock. Solar wind electron velocity distributions in the upstream region of the terrestrial bow shock are characterized by a counterstream structure and a thermalization of backstreaming electrons attributed to the heating at the bow shock (*Feldman et al.* [1983a]). The orientation of the estimated magnetic field is also consistent with this interpretation if we consider $\pm 20^\circ$ ambiguity of our estimation. This can be applied to the other cases similar to event 2 observed from 0745 UT to 0755 UT which were explained earlier.

The other possibility is that the solar wind electrons are thermalized and reflected in the lunar downstream region. It is expected that there is a region of the ion beam disruption in the central part of the lunar wake beyond the distance of $\sim$20 R_L from the center of the Moon (*Farrell et al.* [1998]). There is a possibility that electrons are heated owing to the plasma instability associated with the ion beam disruption and escape out of the wake having characteristics similar to the backstreaming electrons from the Earth's bow shock.

Section 4.5
Summary

Observations by the PSA/ESA on board the NOZOMI spacecraft around the time of the NOZOMI lunar swing-by on Dec. 18, 1998 showed backstreaming electron enhancements in relatively high energy ranges. We classified these events into two types by the characteristics of the electron velocity distribution. Event 1 was observed during 0724 UT and 0736 UT, and event 2 was observed around 0743 UT and 0745-0755 UT.

In event 1, the spectrum of backstreaming electrons was very similar to that of solar wind electrons. But the ratio of these electrons in the phase space density has an energy dependence, which can be interpreted by the electron reflection by the ambipolar potential drop in the lunar wake. Because the critical energy of the electron reflection was $\sim$480 eV, the amplitude of the potential drop is concluded to be 480 V.

In event 2, the spectrum of backstreaming electrons had a different feature from the solar wind electrons, and we think the backstreaming electrons originated from the thermalized electrons in a downstream region. There are two possibilities; the terrestrial bow shock and the lunar downtail region where the two-stream instabilities are active. It is difficult to determine the reflection mechanism due to the similarity of the foreshock region and forewake region. Moreover, the magnetic field can be considered to be connected both of the terrestrial bow shock and the lunar wake.

The electrons with energies of the order of 100 eV have information on the activities of the magnetically connected regions. These observations revealed that structures in the lunar wake regions are more active than those previously expected. Understanding the physics of lunar wake enhances our knowledge of the plasma interaction between the solar wind and planetary bodies. Many asteroids or satellites are thought to be in similar conditions.

Chapter 5

Conclusions

We have analyzed plasma velocity distribution in the vicinity of the Moon to understand the plasma environment of the Moon, especially to discuss the interaction of the Moon with the solar wind plasma.

By the analysis of the 3-D distribution functions of ions obtained in the vicinity of the Moon, it is concluded that protons are injected into the interplanetary space from the Moon with fluxes of $10^6 \sim 10^7$/ cm^2 sec. Their source is the dayside region of the Moon, where the magnetic anomalies was mainly distributed during the observation. They were observed only under the specific condition of the solar wind and the spacecraft location relative to the Moon body. They had large initial velocities comparable to, or larger than, those of the solar wind and had the velocity distribution function of a partial ring structure.

Based on these results, we propose the following scenario for lunar ions: the Moon must have a deflector in its vicinity, which deflect a part of the solar wind protons around the lunar surface while most protons are absorbed when they reach the lunar surface. The miniature bow shock, resulting from the interaction between the lunar magnetic anomalies and the solar wind, is the most likely candidate. The first adiabatic invariant is broken during the deflection. The deflected protons have large velocities due to the bulk velocity of the solar wind, and they move under the force exerted by the convection electric field and gyrate around the magnetic field. This motion forms a partial ring structure with large initial velocities in the velocity phase space as observed by the PSA/ISA. The observation of nonthermal ions proves that a dynamic electromagnetic structure exists in front of the Moon.

The electron distribution functions in the vicinity of the Moon are also discussed. The electrons have information on the region magnetically connected to the spacecraft. When NOZOMI spacecraft was close to the Moon, the flux of the backstreaming electrons with energies larger than 80 eV enhanced. It lasted for about 30 min and the intervals can be divided into two types by the characteristics of the electron distribution functions.

In the first event, the spectrum of backstreaming electrons was very similar to that of solar wind electrons. This means that the solar wind electrons are reflected by the electrostatic potential in the downstream region along the magnetic field. The magnetic field was connected to the void region during the event, so that the possible source of the backstreaming electrons is the ambipolar potential drops formed at the edge of the void region. Because the critical energy of the electron reflection was $\sim$480 eV, the amplitude of the potential drop is concluded to be 480 V.

In the second event, the spectrum of backstreaming electrons had a different feature from the solar wind electrons, so that the backstreaming electrons are originated from the thermalized electrons in a downstream region. Two possible reflection mechanisms are possible; the terrestrial bow shock and the lunar downtail region where the two-stream instabilities are acting. It is difficult to determine which reflection mechanism is responsible because the magnetic field can be considered to be connected both to the terrestrial bow shock and to the lunar wake. In addition, the foreshock region and forewake region have very similar structure.

The observation by modern instruments on board NOZOMI revealed detailed structure of lunar plasma environment. The ion observations proved the existence of dynamic structures in front of the Moon. The structures are thought to be related to the locally magnetized regions of crustal origin. Our results motivate the theories and numerical modellings of the solar wind interaction with small-scale magnetized region, of which scale is almost of the same order to the gyro-radius of the solar wind protons.

The electron observations detected the large electrostatic potential in the lunar downstream region. The value of 480 V is larger than the current value of ∼40 V by numerical calculations. The discrepancy may result from some assumptions made in the calculations. Further studies with more accurate model are necessary for understanding the physics of the lunar wake.

References

Asbridge, J. R., S. J. Bame, and I. B. Strong, Outward flow of protons from the earth's bow shock, *J. Geophys. Res.*, *73*, 5777–5782, 1968.

Benson, J., J. W. Freeman, and H. K. Hills, The lunar terminator ionosphere, *Proc. Lunar. Sci. Conf.*, *6th*, 3013–3021, 1975.

Birch, P. C., and S. C. Chapman, Detailed structure and dynamics in particle-in-cell simulations of the lunar wake, *Phys. Plasmas*, *8*, 4551–4559, 2001.

Bosqued, J. M., N. Lormant, H. R. andC. d'Uston, R. P. Lin, K. A. Anderson, C. W. Carlson, R. E. Ergun, D. Larson, J. McFadden, M. P. Carthy, G. K. Parks, T. R. Sanderson, and K. P. Wenzel, Moon-solar wind interaction: First results from the wind/3dp experiment, *Geophys. Res. Lett.*, *23*, 1259–1262, 1996.

Cladis, J. B., W. E. Francis, and R. R. Vondrak, Transport toward earth of ions sputtered from the moon's surface by the solar wind, *J. Geophys. Res.*, *99*, 53–64, 1994.

Colburn, D. S., R. G. Currie, J. D. Mihalov, and C. P. Sonett, Diamagnetic solar-wind cavity discovered behind the moon, *Science*, *158*, 1040–1042, 1967.

Colburn, D. S., J. D. Mihalov, and C. P. Sonett, Magnetic observations of the lunar cavity, *J. Geophys. Res.*, *76*, 2940–2957, 1971.

Coleman Jr., P. J., C. T. Russel, L. R. Sharp, and G. Schubert, Preliminary mapping of the lunar magnetic field, *Phys. Earth Planet. Interiors*, *6*, 167–174, 1972.

Davis, L., and E. J. Smith, The in-flight determination of spacecraft magnetic field zeros, *Trans. AGU*, *49*, 257, 1968.

Dolginov, S. S., Y. G. Yeroshenko, L. N. Zhuzgov, N. V. Pushkov, and L. O. Tyurmina, Measuring the magnetic fields of the earth and moon by means of sputnik

3 and space rockets 1 and 2, *Space Res.*, *1*, 863–868, 1960.

Dolginov, S. S., Y. G. Yeroshenko, L. N. Zhuzgov, and N. V. Pushkov, Measurements of the magnetic field near the moon by the lunar 10 orbiter, *Dokl. Acad. Sci. USSR, Earth Sci. Sect.*, *170*, 18–20, 1966.

Dyal, P. C., W. Parkin, and W. D. Daily, Surface magnetometer exmhperiments: Internal lunar proerties, *Proc. Lunar Sci. Conf. 4th*, p. 2229, 1973.

Farrell, W. M., R. J. Fitzenreiter, C. J. Owen, J. B. Byrnes, R. P. Lepping, K. W. Ogilvie, and F. Neubauer, Upstream ULF waves and energetic electrons associated with the lunar wake: Detection of precursor activity, *Geophys. Res. Lett.*, *23*, 1271–1274, 1996.

Farrell, W. M., M. L. Kaiser, J. T. Steinberg, and S. D. Bale, A simple simulation of a plasma void: Applications to Wind observations of the lunar wake, *J. Geophys. Res.*, *103*, 23,653–23,660, 1998.

Feldman, W. C., J. R. Asbridge, S. J. Bame, M. D. Montgomery, and S. P. Gary, Solar wind electrons, *J. Geophys. Res.*, *80*, 4181–4196, 1975.

Feldman, W. C., R. C. Anderson, S. J. Bame, S. P. Gary, J. T. Gosling, D. J. McComas, and M. F. Thomsen, Electron velocity distributions near the earth's bow shock, *J. Geophys. Res.*, *88*, 96–110, 1983a.

Feldman, W. C., R. C. Anderson, S. J. Bame, J. T. Gosling, R. D. Zwickl, and E. J. Smith, Electron velocity distributions near the interplanetary shocks, *J. Geophys. Res.*, *88*, 9949–9958, 1983b.

Gringaus, K. I., V. V. Bezrukikh, M. Z. Khokhlov, G. N. Zastenker, A. P. Remizov, and L. S. Musatov, Study of plasma in the neighborhood of the moon using charged-particle traps on the first lunar artificial satellite, *Cosmic Res.*, *4*, 736–750, 1966.

Harnett, E. M., and R. Winglee, Two-dimensional MHD simulation of the solar wind interaction with magnetic field anomalies on the surface of the moon, *J. Geophys. Res.*, *105*, 24,997–25,007, 2000.

Hilchenbach, M., D. Hovestadt, B. Klecker, and E. Möbius, Observation of energetic lunar pick-up ions near earth, *Adv. Space Res.*, *13*, (10)321–(10)324, 1993.

Hinchenbach, M., D. Hovestadt, B. Klecker, and E. M̈bius, Detection of singly ionized energetic lunar pick-up ions upstream of Earth's bow shock, in *Proceedings Solar Wind Seven*, edited by E. Marsch and G. Schwenn, pp. 349–355, Pergamon Press, Gosler Germany, 1991.

Hood, L. L., and Z. Huang, Formation of magnetic anomalies antipodal to lunar impact basi ns: Two-dimensional model calculations, *J. Geophys. Res.*, *96*, 9837–9846, 1991.

Hood, L. L., and C. R. Williams, The lunar swirls: Distribution and possible origins, *Proc. 19th Lunar Planet. Sci. Conf.*, pp. 99–113, 1989.

Hood, L. L., D. L. Mitchell, R. P. Lin, M. H. A. na, and A. B. Binder, Initial measurements of the lunar-induced magnetic dipole moment using lunar prospector magnetometer data, *Geophys. Res. Lett.*, *26*, 2327–2330, 1999.

Hood, L. L., A. Zakharian, J. Halekas, D. L. Mitchell, R. P. Lin, M. H. Acuña, and A. B. Binder, Initial mapping and interpretation of lunar crustal magnetic anomalies using Lunar Prospector magnetometer data, *J. Geophys. Res.*, *106*, 27,825–27,839, 2001.

Lin, R. P., D. L. Mitchell, D. W. Curtis, K. A. Anderson, C. W. Carlson, J. McFadden, M. H. A. na, L. L. Hood, and A. Binder, Lunar surface magnetic fields and their interaction with the solar wind: Results from lunar prospector, *Science*, *281*, 1480, 1998.

Lundin, R., A. Zakharov, R. Pellinen, H. Borg, B. Hultqvist, N. Pissarenko, E. M. Dubinin, S. W. Barabash, I. Liede, and H. Koskinen, First measurements of the ionospheric plasma escape from mars, *Nature*, *341*, 609–612, 1989.

Lyon, E. F., H. S. Bridge, and J. H. Binsack, Explorer 35 plasma measurements in the vicinity of the moon, *J. Geophys. Res.*, *72*, 6113–6117, 1967.

Machida, S., Y. Saito, Y. Ito, and H. Hayakawa, Instrumental characteristics of Electron Spectrum Analyzer (ESA) onboard the planet-b mission and observational perspectives of the electron measurements, *Earth Planets Space*, *50*, 207–211, 1998.

Mall, U., E. Kirsch, K. Cierpka, B. Wilken, A. Söding, F. Neubauer, G. Gloeckler, and A. Galvin, Direct observation of lunar pick-up ions near the moon, *Geophys. Res. Lett.*, *25*, 3799–3802, 1998.

Michel, F. C., Interaction between the solar wind and a lunar atmosphere, *Planet. Space Sci.*, *12*, 1075–1091, 1964.

Michel, F. C., Magnetic field structure behind the moon, *J. Geophys. Res.*, *73*, 1533–1542, 1968.

Mihalov, J. D., and A. Barnes, Evidence for the acceleration of ionosphereic O^+ in the magnetosheath of Venus, *Geophys. Res. Lett.*, *8*, 1277–1280, 1981.

Mihalov, J. D., C. P. Sonett, J. H. Binsack, and M. D. Moutsoulos, Possible fossil lunar magnetism inferred from satellite data, *Science*, *171*, 892–895, 1971.

Möbius, E., D. Hovestadt, B. Klecker, M. Scholer, G. Gloeckler, and F. M. Ipavich, Direct observation of He^+ pick-up ions of interstellar origin in the solar wind, *Nature*, *318*, 426–429, 1985.

Mukai, T., W. Miyake, T. Terasawa, M. Kitayama, and K. Hirao, Plasma observation by Suisei of solar-wind interaction with comet halley, *Nature*, *321*, 299–303, 1986.

Ness, N. F., K. W. Behannon, C. S. Scearce, and S. C. Cantarano, Early results form the magnetic field experiment on Lunar Explorer 35, *J. Geophys. Res.*, *72*, 5769–5778, 1967.

Ness, N. F., K. W. Behannon, H. E. Taylor, and Y. C. Whang, Perturbations of the interplanetary magnetic field by the lunar wake, *J. Geophys. Res.*, *73*, 3421–3440, 1968.

Noda, H., T. Terasawa, Y. Saito, H. Hayakawa, A. Matsuoka, and T. Mukai, Observation of the interstellar helium cone by NOZOMI spacecraft, *Space Sci. Rev.*, 2001.

Ogilvie, K. W., J. T. Steinberg, R. J. Fitzenreiter, C. J. Owen, A. J. Lazarus, W. M. Farrell, and R. B. Torbert, Observation of the lunar plasma wake from the wind spacecraft on dec. 27, 1994, *Geophys. Res. Lett.*, *23*, 1255–1258, 1996.

Ogilvie, K. W., L. F. Burlaga, D. J. Chornay, and R. J. Fitzenreiter, Source of the solar wind electron strahl in 1995, *J. Geophys. Res.*, *104*, 22,389–22,393, 1999.

Paschmann, G., N. Sckopke, I. Papamastorakis, J. R. Asbridge, S. J. Bame, and J. T. Gosling, Characteristics of reflected and diffuse ions upstream from the Earth's bow shock, *J. Geophys. Res.*, *86*, 4355–4364, 1981.

Peredo, M., J. A. Slavin, E. Mazur, and S. A. Curtis, Three-dimensional position and shape of the bow shock and their variation with Alfvénic, sonic and magnetosonic mach numbers and interplanetary magnetic field orientation, *J. Geophys. Res.*, *100*, 7907–7916, 1995.

Reasoner, D. L., and W. J. Burke, Characteristics of the lunar photoelectron layer while in the geomagnetic tail, in *Proceedings Sixth ESLAB Symposium*, pp. 26–29, Eur. Space Res. and Technol.Center, Noordwijk, Netherlands, 1972.

Russell, C. T., and B. R. Lichtenstein, On the source of lunar limb compresseions, *J. Geophys. Res.*, *80*, 4700–4711, 1975.

Samir, U., K. H. Write, Jr., and N. H. Stone, The expansion of plasma into a vacuum: basic phenomena and processes and applications to space plasma physics, *Rev. Geophys. and Space Phys.*, *21*, 1631–1646, 1983.

Schubert, G., and B. R. Lichtenstein, Observations of moon-plasma interactions by orbital and surface experiments, *Rev. Geophys. Space Phys.*, *12*, 592–626, 1974.

Sharp, L. R., P. J. Coleman Jr., B. R. Lichtenstein, C. T. Russell, and G. Schubert, Orbital mapping of the lunar magnetic field, *Moon*, *7*, 322, 1973.

Sonett, C. P., and J. D. Mihalov, Lunar fossil magnetism and perturbations of the solar wind, *J. Geophys. Res.*, *77*, 588–603, 1972.

Sonett, C. P., D. S. Colburn, and R. G. Currie, The intrinsic magnetic field of the moo, *J. Geophys. Res.*, *72*, 5503–5507, 1967.

Stern, S. A., The lunar atmosphere: History, status, current problems and context, *Rev. Geophys.*, *37*, 453–491, 1999.

Taylor, H. E., K. W. Behannon, and N. F. Ness, Measurements of the perturbed interplanetary magnetic field in the lunar wake, *J. Geophys. Res.*, *73*, 6723–6735, 1968.

Terasawa, T., T. Mukai, W. Miyake, M. Kitayama, and K. Hirao, Detection of cometary pickup ions up to 10^7 km from comet Halley: Suisei observation, *Geophys. Res. Lett.*, *13*, 837–840, 1986.

Thomsen, M. F., Upstream suprathermal ions, in *Collisionless shocks in the heliosphere: Revies of current research*, edited by B. T. Tsurutani and R. G. Stone, pp. 253–270, American Geophysical Union, 1985.

Vyshlov, A. S., Preliminary results of circumlunar plasma research by luna 22 spacecraft, *Space Res.*, *XVI*, 945–949, 1976.

Whang, Y. C., and N. F. Ness, Mangetic-field anomalies in the lunar wake, *J. Geophys. Res.*, *77*, 1109–1115, 1972.

Yamamoto, T., and A. Matsuoka, Planet-b magnetic fields investigation, *Earth Planets Space*, *50*, 189–194, 1998.

This thesis was written on the basis of the following papers;

1. Y. Futaana, S. Machida, Y. Saito, A. Matsuoka, and H. Hayakawa, Counterstreaming electrons in the near vicinity of the Moon observed by plasma instruments on board NOZOMI, *J. Geophys. Res.*, *106*, 18729-18740, 2001.

2. Y. Futaana, S. Machida, Y. Saito, A. Matsuoka, and H. Hayakawa, Moon-related nonthermal ions observed by NOZOMI: Species, sources, and generation mechanisms, *J. Geophys. Res.*, *108*, A1, doi: 10.1029/2002JA009366, 2003.